

1 Retrieval of nearshore bathymetry from Landsat 8 images: a tool for 2 coastal monitoring in shallow waters

3 Pacheco, A.¹, Horta, J.¹, Loureiro, C.^{1,2,3}, Ferreira, Ó.¹

4 ¹CIMA/Universidade do Algarve, Edifício 7, Campus de Gambelas Faro, 8005-139, Portugal,

5 ²Marine Geology Research Unit, School of Agriculture, Earth and Environmental Sciences, University of KwaZulu-
6 Natal, Westville Campus, Private Bag X54001, Durban, South Africa

7 ³Environmental Sciences Research Institute, School of Environmental Sciences, University of Ulster, Coleraine,
8 BT52 1SA, United Kingdom

9 ampacheco@ualg.pt, jphorta@ualg.pt, cloureiro@ualg.pt, oferreir@ualg.pt
10

11 Abstract

12 Nearshore bathymetry is likely to be the coastal variable that most limits the
13 investigation of coastal processes and the accuracy of numerical models in coastal areas,
14 as acquiring medium spatial resolution data in the nearshore is highly demanding and
15 costly. As such, the ability to derive bathymetry using remote sensing techniques is a
16 topic of increasing interest in coastal monitoring and research. This contribution focuses
17 on the application of the linear transform algorithm to obtain satellite-derived
18 bathymetry (SDB) maps of the nearshore, at medium resolution (30 m), from freely
19 available and easily accessible Landsat 8 imagery. The algorithm was tuned with
20 available bathymetric Light Detection and Ranging (LiDAR) data for a 60-km-long
21 nearshore stretch of a highly complex coastal system that includes barrier islands,
22 exposed sandy beaches, and tidal inlets (Ria Formosa, Portugal). A comparison of the
23 retrieved depths is presented, enabling the configuration of nearshore profiles and
24 extracted isobaths to be explored and compared with traditional
25 topographic/bathymetric techniques (e.g., high- and medium-resolution LiDAR data and
26 survey-grade echo-sounding combined with high-precision positioning systems). The
27 results demonstrate that the linear algorithm is efficient for retrieving bathymetry from
28 multi-spectral satellite data for shallow water depths (0 to 12 m), showing a mean bias
29 of -0.2 m, a median difference of -0.1 m, and a root mean square error of 0.89 m.
30 Accuracy is shown to be depth dependent, an inherent limitation of passive optical
31 detection systems. Accuracy further decreases in areas where turbidity is likely to be
32 higher, such as locations adjacent to tidal inlets. The SDB maps provide reliable
33 estimations of the shoreline position and of nearshore isobaths for different cases along
34 the complex coastline analysed. The use of freely available satellite imagery proved to
35 be a quick and reliable method for acquiring updated medium-resolution, high-

36 frequency (days and weeks), low-cost bathymetric information for large areas and
37 depths of up to 12 m in clear waters without wave breaking, allowing almost constant
38 monitoring of the submerged beach and the shoreface.

39

40 **Keywords:** Satellite-derived bathymetry; Landsat; LiDAR; linear transform algorithm;
41 coastal monitoring; Ria Formosa

42

43 **1. Introduction**

44 Updated and detailed coastal topography and bathymetry are increasingly being
45 required for a wide variety of purposes including research, management, and marine
46 spatial planning. With the expansion of coastal and marine economic activities, there is
47 a growing need to develop fast and accurate measurements of nearshore regions, as well
48 as to describe the physical features of the sea bottom and adjoining coastal areas,
49 particularly for the purposes of modelling and monitoring. Coastal observation systems
50 continue to be developed for measuring parameters of and processes related to water
51 quality, hydrodynamics, meteorology, and ecology, as well as submarine
52 geomorphology (analysed using bathymetric data).

53 Accurate bathymetries are the most essential data for driving coastal modelling and
54 monitoring. Currently, two of the most widely used techniques for acquiring
55 bathymetric data rely on single- or multi-beam echo-sounding and airborne Light
56 Detection and Ranging (LiDAR). However, the cost and logistical difficulties of
57 obtaining nearshore bathymetry using these methods makes survey updates rare or
58 allows them to be conducted only on sites of special interest. As such, the ability to
59 derive continuous bathymetry from satellite images has become a topic of increased
60 interest for coastal monitoring. Such an approach exploits the fact that different
61 wavelengths of the light spectrum are attenuated by water to varying degrees. Initially,
62 these approaches could not be used for marine mapping applications owing to the
63 unique optical properties of water and to highly variable parameters such as turbidity.
64 However, advances in the optical sensors on board remote sensing satellite platforms
65 have improved the ability to detect the spectral properties of aquatic targets such as
66 bottom reflectance, which can then be inverted to yield direct estimates of depth
67 (Mobley et al., 2005).

68 The present work explores the retrieval of satellite-derived bathymetry (SDB) for
69 shallow coastal areas, aiming to provide a straightforward and inexpensive method for
70 obtaining and updating bathymetric data relevant to coastal research and management.
71 The study takes advantage of several improvements introduced in the latest generation
72 of Landsat imagery that were included in the Landsat 8 mission launched in early 2013.
73 Furthermore, the Landsat 8 satellite images the entire Earth at approximately fortnightly
74 intervals (every 16 days) and the data collected by the instruments onboard the satellite
75 are available to download at no charge. This paper details the processing of the satellite
76 images required to derive bathymetric maps using the water radiance of three bands
77 (coastal aerosol: 433–453 nm; blue: 450–515 nm; and green: 525–600 nm). The
78 processing steps include the radiometric rescaling of the images, the application of
79 adapted Lyzenga's (1985) depth-retrieval algorithm that uses existing bathymetric data
80 for tuning the image-to-depth conversion, and an averaged and depth-dedicated error
81 analysis. The SDB maps generated have medium resolution (~30 m) and are used to
82 provide cost-effective, frequent, high-density data in raster map format.

83

84 **2. Study area**

85 The nearshore coastal waters adjacent to the Ria Formosa system in southern Portugal
86 were chosen as the test case in which to derive satellite bathymetric maps (Fig. 1A)
87 because of the complexity and variability of this coastal environment. The Ria Formosa
88 is a coastal lagoon bordered by a multi-inlet barrier island system, and the adjacent
89 coastal areas have several different morphologies such as tidal inlets, alongshore bars,
90 crescentic bars, shoals, and ebb channels. The total length of the system is 60 km,
91 presently comprising five islands and two peninsulas separated by six tidal inlets. The
92 inlets comprise three artificially opened or relocated inlets (Ancão, Fusetas, and Lacém),
93 two artificially stabilised inlets (Faro–Olhão and Tavira), and one natural inlet
94 (Armona). Tides in the area are semi-diurnal, with average ranges of 2.8 m and 1.3 m
95 for spring and neap tides, respectively. Maximum ranges of 3.5 m can be reached during
96 spring tides. Wave energy is moderate with an average annual offshore significant wave
97 height (H_s) of 1.0 m and an average peak period (T_p) of 8.2 s. Dominant incident waves
98 are from the W–SW, representing 71% of occurrences, although E–SE conditions
99 represent 23% of the observations (Costa et al., 2001). Net littoral drift and alongshore
100 currents are typically from west to east. The cusped shape of this coastal area induces

101 two behaviours in terms of exposure to wave action: the west coast is more energetic,
 102 being under the direct influence of the dominant wave conditions (W–SW), whereas the
 103 east coast is directly exposed only to the E–SE waves. The nearshore morphology also
 104 reflects this cusped shape, with the bathymetry being generally shore parallel, although
 105 incorporating complex areas such as shoals, ebb deltas, alongshore and swash bars, and
 106 ridge and runnel systems (Pacheco et al., 2011).

107

108 3. METHODS

109 3.1. Physical assumptions

110 The physical concept underlying the ability to estimate bathymetry from multi-spectral
 111 imagery is the wavelength-dependent attenuation of light in the water column. The
 112 transformation of subsurface reflectance to the bottom albedo is based on analytical
 113 equations for irradiance reflectance (R) and remote-sensing reflectance (R_{rs}) for both
 114 deep- and shallow-water applications parameterised by Albert and Mobley (2003). In
 115 shallow waters, R_{rs} is the fundamental property for the inversion of subsurface
 116 properties such as water depth or bottom composition. R_{rs} depends not only on the
 117 absorption and scattering properties of dissolved and suspended material in the water
 118 column, but also on the bottom depth (d_b) and the reflectivity of the bottom, or the
 119 bottom albedo (R_B) (Albert & Mobley, 2003; Dekker et al., 2011). The spectral R_{rs} is
 120 given by:

121

$$122 \quad R_{rs}(\lambda) = f[a(\lambda), b_b(\lambda), R_B(\lambda), d_b, \theta_w, \theta_v, \varphi] \quad (1)$$

123 where $a(\lambda)$ is the absorption coefficient, $b_b(\lambda)$ is the backscatter coefficient, $R_B(\lambda)$ is
 124 the benthic spectral reflectance (i.e., bottom albedo), d_b is the bottom depth, θ_w is the
 125 sub-surface solar zenith angle, θ_v is the sub-surface viewing angle from nadir, and φ is
 126 the viewing azimuth angle from the solar plane. The result is a complete set of
 127 analytical equations for the remote sensing signals R and R_{rs} in both deep and shallow
 128 waters (Albert and Mobley, 2003; Albert and Gege, 2006). The input variables for the
 129 parameterisation are the inherent optical properties of the water mentioned above, that
 130 is, $a(\lambda)$ and $b_b(\lambda)$. Additionally, θ_w and θ_v are considered.

131

132 **3.2. Dataset**

133 The Landsat 8 satellite images consist of 11 spectral bands providing moderate-
134 resolution (15–100 m) imagery of Earth’s land surface. The spatial resolution of the
135 spectral bands is 30 m for Bands 1 to 7 and 9, 15 m for Band 8 (panchromatic), and
136 100 m for Bands 10 and 11. The approximate scene size is 170 km north–south by 183
137 km east–west. Landsat 8 has many differences compared with previous Landsat
138 missions. Particularly relevant was the introduction of the new band 1 (ultra-blue and/or
139 coastal aerosol), which is useful for coastal studies. Further details on Landsat 8
140 products and scientific applications can be found in Roy et al. (2014). The standard
141 Landsat 8 products provided by the United States Geological Survey (USGS) consist of
142 quantised and calibrated Digital Numbers (DNs) representing multi-spectral image data
143 acquired with both the Operational Land Imager (OLI) and the Thermal Infra-Red
144 Sensor (TIRS). The products are delivered in 16-bit unsigned integer format and can be
145 rescaled to Top Of Atmosphere (TOA) reflectance and/or radiance using radiometric
146 rescaling coefficients provided in the product metadata file (MTL file). Two satellite
147 scenes from April and June 2013 were downloaded based on survey time, geographic
148 extent, and environmental conditions (e.g., an absence of cloud cover), and were
149 georeferenced to the WGS84 datum, UTM projection Zone 29 (Table 1).

150 To tune the satellite image-to-depth conversion, up-to-date and detailed bathymetric
151 information was obtained from the May 2011 topographic–bathymetric LiDAR dataset
152 of the Portuguese coast, with the subset of waters in the Ria Formosa system being of
153 particular interest (Table 1). The combined topographic and bathymetric LiDAR
154 datasets were assembled to produce a model of the Portuguese coastal areas with 2-m
155 resolution from 0 to 12 m depth, confirmed to Order 1A of the International
156 Hydrographic Organisation standards s44 (2008). For the present study, XY positions
157 from all the acquired survey data were also projected using UTM Zone 29, referred to
158 the GRS 80 ellipsoid and to the WGS84 datum. Depth (Z) measurements were referred
159 to mean sea level (MSL).

160

161 **3.3. Depth-retrieval algorithm**

162 The method that was used to derive bathymetry from variable bottom types is an
163 adapted version of the linear transform bathymetry algorithm originally developed by

164 Lyzenga (1978, 1985) and was applied to the Landsat 8 scene to match with the
 165 available LiDAR bathymetric reference dataset. The method uses the reflectance for
 166 each satellite imagery band, calculated with the sensor calibration files and corrected for
 167 atmospheric effects. The reflectance of water (R_w), which includes the bottom where
 168 the water is optically shallow, is given by:

169

$$170 \quad R_w = \frac{\pi L_w(\lambda)}{E_d(\lambda)} \quad (2)$$

171 where L_w is the water-leaving radiance, E_d is the downwelling irradiance entering the
 172 water, and λ is the spectral band. L_w and R_w refer to values above the water surface.
 173 R_w is determined by correcting the total reflectance R_T for aerosol and surface
 174 reflectance, as estimated by the near-IR band, and for the Rayleigh reflectance R_r by:

175

$$176 \quad R_w = R_T(\lambda_i) - Y(\lambda_i)R_T(\lambda_{IR}) - R_r(\lambda_i) \quad (3)$$

177 where Y is the constant to correct the spectral variation and is aerosol dependent,
 178 subscript i denotes a visible channel, and subscript IR denotes the near-IR (NIR)
 179 channel. R_T is found by:

180

$$181 \quad R_T(\lambda_i) = \frac{\pi L_T(\lambda_i)/E_0(\lambda_i)}{(1/r^2)T_0(\lambda_i)T_1(\lambda_i)\cos\theta_0} \quad (4)$$

182 where L_T is the (total) radiance measured at the satellite, E_0 is the solar constant, r is
 183 the Earth–Sun distance in astronomical units, θ_0 is the solar zenith angle, and T_0 and T_1
 184 are the transmission coefficients for Sun-to-Earth and Earth-to-satellite, respectively
 185 (Stumpf et al., 2003).

186 The atmosphere has a significant impact on satellite data, such as information loss,
 187 caused by scattering by atmospheric constituents and aerosols. Atmospheric correction
 188 over coastal waters is particularly challenging because of the much lower signal-to-
 189 noise ratio (SNR) compared with that of land. Consequently, water-specific Landsat 8
 190 atmospheric correction techniques are being developed that take advantage of the new
 191 shorter-wavelength coastal blue band (Roy et al., 2014).

192 For Landsat 8, the number of steps necessary in the atmospheric correction process can
 193 be reduced when compared with previous Landsat missions because terms have been
 194 embedded in Landsat 8 DN values. For the present paper, atmospheric corrections were
 195 performed using the Dark Object Subtraction (DOS) method. DOS assumes that dark
 196 objects (e.g., deep water and shadows) have near-zero-percent reflectance. Thus, the
 197 signal recorded by the sensor from these features includes a substantial component of
 198 atmospheric scattering, which must be removed (Chavez, 1988, 1996). The basic
 199 assumption is that within the image, some pixels are in complete shadow and their
 200 radiances received at the satellite are due to atmospheric scattering (i.e., path radiance,
 201 Chavez, 1996). This assumption is combined with the fact that very few targets on
 202 Earth's surface are absolutely black. In the present study, the minimum scatter radiance
 203 (i.e., the 1% radiance of a dark object) was determined (Nazeer et al., 2014) as:

204

$$205 \quad L_{1\%} = \frac{0.01E_{sun\lambda_i}\cos\theta_0}{\pi d^2} \quad (5)$$

206 where $E_{sun\lambda_i}$ is the exo-atmospheric solar irradiance for band λ_i ($\text{Wm}^{-2}\mu\text{m}^{-1}$), and d is
 207 the Earth–Sun distance (in astronomical units). The value $L_{1\%}$ was then subtracted from
 208 each corresponding $L_T(\lambda_i)$ to remove the path radiance. This method has an advantage
 209 over other methods as it does not require any in situ atmospheric information and has
 210 been consistently used for atmospheric corrections of multi-spectral imagery in diverse
 211 coastal settings (Keith et al., 2014). Recent evaluations have confirmed the performance
 212 of the DOS method for precise atmospheric corrections of Landsat imagery over coastal
 213 areas (Nazeer et al., 2014).

214 Following Lyzenga (1978, 1985) and Stumpf et al. (2003), two or more bands can
 215 provide an independent correction for bottom albedo in finding the depth as well as a
 216 linear solution between satellite-derived depth (Z_{LSat8}) and water reflectance, which is
 217 given by:

218

$$219 \quad Z_{LSat8} = a_0 + a_i(X_i) + a_j(X_j) + a_k(X_k) \quad (6)$$

220 where

$$221 \quad X_i = \ln [R_w(\lambda_i) - R_\infty(\lambda_i)] \quad (7)$$

$$222 \quad X_j = \ln [R_w(\lambda_j) - R_\infty(\lambda_i)] \quad (8)$$

$$223 \quad X_k = \ln [R_w(\lambda_k) - R_\infty(\lambda_i)] \quad (9)$$

224 where R_∞ is the water column reflectance in the case where the water is optically deep
 225 (presumed to be $\min(R_w)$ in optically deep water, following Lyzenga, 1985). R_∞ and the
 226 constants a_0 , a_i , a_j , and a_k are determined by multiple linear regression computed
 227 using the LiDAR bathymetric data (Z_{LiDAR}) for depths of 0–12 m; i , j , and k are the
 228 indices representing the coastal aerosol, blue, and green bands (λ) of Landsat 8 scenes,
 229 respectively.

230 To apply the multiple linear regression, the LiDAR data from May 2011 were extracted
 231 for the entire nearshore Ria Formosa area with 30-m resolution at exactly the same
 232 points as were the data retrieved by the Landsat 8 image of June 2013, comprising a
 233 total of 35,247 points (N). A limitation of this comparison is the fact that Landsat 8
 234 scenes of Ria Formosa have been available only since early 2013, whereas the depth-
 235 retrieval linear algorithm applied to the Landsat 8 June 2013 scenes to derive the SDB
 236 maps was tuned with a LiDAR bathymetric dataset from May 2011; that is, there is a 2-
 237 year difference. Therefore, a perfect agreement between SDB and LiDAR maps is not
 238 expected, given that morphological differences are likely to occur in a moderately
 239 energetic nearshore system comprising barrier islands and tidal inlets exposed to
 240 dynamic oceanographic conditions, and given that (in the case of adjacent areas of tidal
 241 inlets) dredging activities have taken place in the main navigable channels or ebb deltas.
 242 However, the number of points (N) retrieved and the fact that the analysis covers a 60-
 243 km-long coastal stretch ensure the robustness of the statistical comparison as a large
 244 number of Z points extracted at medium resolution are expected to remain unchanged.
 245 Moreover, the satellite image and the LiDAR data were both obtained in late spring
 246 (June 2013 and May 2011, respectively), implying that the main morphologies should
 247 be adjusted to similar energy conditions.

248 LiDAR data points were referenced to MSL and were tide corrected, but the satellite
 249 image was acquired at a particular date and time. As such, a corresponding tide offset
 250 needs to be corrected before applying the regression model to obtain model coefficients.
 251 The correction of the satellite image was performed by matching the image time with
 252 tidal level using a tidal predictor (Pawlowicz et al., 2002). The processing steps are
 253 illustrated in Fig. 2.

254 3.4. Data analysis

255 The satellite-derived depths (Z_{LSat8}) were compared against the LiDAR depths (Z_{LiDAR})
 256 and separated into depth ranges (Table 2 and Fig. 3). The differences between Z_{LSat8}
 257 and Z_{LiDAR} were then analysed statistically (Table 2 and Fig. 4) and plotted against the
 258 X coordinate to evaluate their spatial variation throughout the study area (Fig. 3).
 259 During the calibration stage, and to better understand the coastal morphologies that
 260 SDB with a resolution of 30 m could distinguish, bathymetric charts were derived for
 261 particular areas of interest (AoI). AoI1 represents the Ancão Peninsula (Fig. 1) and
 262 includes: Bm1, a bathymetric map with 2-m resolution using the LiDAR high-resolution
 263 data (Fig. 5A); Bm2, a bathymetric map with 30-m resolution obtained from a
 264 resampling of the LiDAR data, which constitutes the reference dataset used for
 265 determining the constants a_0 , a_i , a_j , and a_k in the multiple linear regression (Eq. 6 and
 266 Fig. 5B); and Bm3, the SDB map (Fig. 5C).

267 The same interpolator was used to grid the bathymetric maps within the same limits and
 268 resolution following quality controls suggested by Hicks and Hume (1997). Differences
 269 between Bm2 and Bm3 were then determined by applying the difference map method
 270 (DMM) described by Stauble (1998) (Fig. 5D). The DMM is a straightforward method
 271 for computing vertical changes in cells by subtracting two comparison surfaces. An
 272 output map (hereafter referred to as “DMM”) is then created with the differences in Z
 273 between surveys, which is used to evaluate the relative error of the SDB against the
 274 LiDAR survey, namely, by assessing the spatial distribution of error and its association
 275 with specific morphological features (e.g., swash bars, isobaths, and inlet channels).
 276 Complementing this, three descriptive statistical parameters for assessing the overall
 277 performance of the depth-retrieval algorithm were computed (Brando et al., 2009):

278

$$279 \text{Bias}(Z_{LSat8}, Z_{LiDAR}) = \text{mean}(Z_{LSat8}) - \text{mean}(Z_{LiDAR}) \quad (10)$$

$$280 \text{DifMedian}(Z_{LSat8}, Z_{LiDAR}) = \text{median}(Z_{LSat8}) - \text{median}(Z_{LiDAR}) \quad (11)$$

$$281 \text{RMSE}(Z_{LSat8}) = \sqrt{\text{Var}(Z_{LSat8}) + (\text{Bias}(Z_{LSat8}, Z_{LiDAR}))^2} \quad (12)$$

282 where Z_{LiDAR} is the LiDAR depth (from the 30-m-resolution resampled LiDAR dataset)
 283 and Z_{LSat8} is the depth estimated by applying inversion techniques to the Landsat 8
 284 multi-spectral data (i.e., the SDB, Fig. 2). *Bias* (m) and *DifMedian* (m) provide the

285 relative accuracy in the measurement, whereas *RMSE* (Root Mean Square Error, m)
286 includes both random errors (i.e., affecting the precision of the measurement) and
287 systematic errors (i.e., affecting the accuracy of the measurement) (Table 3). Twelve
288 cross-shore profiles spaced every 1000 m (P1 to P12, shown in Fig. 5D) were then
289 extracted from Bm1, Bm2, and Bm3 to evaluate the performance of the SDB map in
290 characterizing the nearshore morphological profile when compared with the high-
291 resolution LiDAR bathymetry (Bm1) and with the coarser grid resolution resample from
292 the LiDAR bathymetric data (Bm2). Such nearshore profiles are represented in Fig. 6,
293 whereas a comparison of the 2-m, 4-m, 6-m, and 8-m isobaths extracted from Bm1,
294 Bm2, and Bm3 is presented in Fig. 7.

295 AoI2 comprises the easternmost area of Tavira Island, the Tavira Inlet, and the
296 westernmost area of Cabanas Island (Fig. 1C), and was chosen for several reasons. First,
297 as mentioned above, Ria Formosa has a cusped shape, and whereas AoI1 faces the
298 prevailing SW oceanographic conditions, AoI2 faces the E-SE conditions. Second,
299 whereas AoI1 encloses an artificially opened inlet that has been allowed to migrate
300 naturally (Ancão Inlet), AoI2 encloses a stabilised inlet with two jetties (Tavira Inlet). A
301 similar procedure to that used for AoI1 was adopted for analysing AoI2, and three
302 bathymetric maps were derived: Bm1, a bathymetric map with 2-m resolution using the
303 LiDAR high-resolution data (Fig. 8A); Bm2, a bathymetric map with 30-m resolution
304 using the resampled LiDAR data (Fig. 8B); and Bm3, the SDB map (Fig. 8C).
305 Differences between Bm2 and Bm3 were then determined by applying the DMM (Fig.
306 8D). Univariate statistics of the DMM for each AoI are presented in Table 3. Because
307 nearshore dynamics and morphological changes are assessed primarily by analysing
308 variation in the nearshore profiles, cross-shore profiles spaced every 1000 m were also
309 extracted from the bathymetric maps (i.e., from Bm1, Bm2, and Bm3) of AoI2 (Fig.
310 8D). The cross-shore nearshore profiles are shown in Fig. 9, and the isobaths extracted
311 from Bm1, Bm2, and Bm3 are displayed in Fig. 10.

312 After calibrating and tuning the coefficients, two validation areas were selected and
313 independently surveyed: AoI3, Barreta Island bathymetry (Fig. 1) obtained on 26 April
314 2013; and AoI4, a bathymetry survey performed on 30 April 2013 at Tavira Inlet. Both
315 bathymetries were compared with SDB maps created using the above-determined
316 coefficients applied to a different Landsat 8 scene obtained for the closest possible date
317 to the surveys (26 April 2013, Table 1). The bathymetries of both AoI3 and AoI4 were

318 established using a Real-Time Kinematics–Differential Global Positioning System
 319 (RTK–DGPS) synchronised with a single-beam survey-grade echo-sounder, the
 320 Echotrac CV100 (Odom Hydrographic System, Inc.) with a 200-kHz transducer. The
 321 echo-sounding bathymetries were performed under fair-weather southwesterly
 322 conditions. The datasets were collected to represent typical environments encountered
 323 in a bathymetric analysis of nearshore and coastal inlets, including complex
 324 morphologies such as ebb deltas and swash bars. Survey lines were spaced 25 m apart,
 325 with survey positions being referenced to the European Terrestrial Reference System
 326 1989 (ETRS89) and depth measurements being referred to MSL. More details on
 327 equipment, data acquisition, and data processing are given by Horta et al. (2014). Both
 328 echo-sounder + RTK–DGPS survey datasets were gridded at Landsat 8' resolution (i.e.,
 329 30 m, Figs 11A and 12A). The SDB maps were determined with the coefficients
 330 calculated using Eq. 6 (Figs. 11B and 12B). For the purpose of comparison, a DMM
 331 grid was produced to determine volumetric variations (Figs 11C and 12C). The spatial
 332 differences between the LiDAR and SDB maps were first evaluated visually by
 333 analysing the elevation-difference maps and afterwards by computing univariate
 334 statistics (Table 3).

335

336 4. Results

337 4.1. Depth-retrieval algorithm

338 The spatial distribution of the residuals ($N = 35,247$) between depths determined using
 339 the depth-retrieval linear algorithm applied to the Landsat 8 scene (June 2013) and those
 340 acquired using LiDAR (May 2011) over 60 km of the nearshore are shown visually in
 341 Fig. 3 and given statistically in Table 2. The depth data were separated into 2-m classes
 342 to allow both methods' strengths and limitations to be distinguished. The distribution of
 343 frequencies was determined to analyse differences between satellite-derived depth
 344 (Z_{LSat8}) and LiDAR depth (Z_{LiDAR}) for each 2-m depth class (Fig. 4). Overall, and for
 345 all depth classes, the distribution of differences is contained within ± 1 m, except for
 346 depths of 10–12 m ($Bias = -1.16$ m; Table 2 and Fig. 4), which is probably related to
 347 the inherent limitations of the bathymetric LiDAR dataset in water depths greater than
 348 10 m resulting from the small number of depth points retrieved ($N = 208$; Fig. 3, Table
 349 2). Maximum and minimum residuals within all depth classes correspond to depth

350 points where the depth-retrieval linear algorithm was ineffective in providing accurate
 351 depth values. Class 1 (Fig. 4 and Table 2), which covers a depth range in which it is
 352 reasonable to expect significant morphological changes over a 2-year period, also had
 353 higher values of *Bias* (0.61 m), *DifMedian* (0.60 m), and *RMSE* (0.94 m). It is also
 354 within this class that a lower accuracy of the depth-retrieval method is expected because
 355 of the stirring of suspended sediment and increased turbidity related to wave breaking.
 356 The *Bias* decreases to values close to 0 for Class 2 (*Bias* = 0.01 m, 2–4 m) and Class 3
 357 (*Bias* = -0.07 m, 4–6 m), increasing to -0.26 m for Class 4 (6–8 m) and -0.31 m for
 358 Class 5 (8–10 m) (Table 2 and Fig. 4). *Bias* and *DifMedian*, the measures of precision,
 359 do not change much for Classes 1–4 but Class 5 presents a very low *DifMedian*
 360 (-0.02 m) when compared with the *Bias* (-0.31 m), which indicates that outliers affect
 361 the *Bias* within this depth class more than in other classes (Table 2). The four classes
 362 comprising the depth range of 2–10 m (Classes 2 to 5) include 82% of the N sampled
 363 points (Fig. 4), whereas Class 1 contains 17% of the points. The spread in the data
 364 points can be evaluated by the variance (*Var*), which measures how far apart are the
 365 depth values retrieved using the linear algorithm from the corresponding LiDAR depths.
 366 Using all data except those in Class 6, which represents less than 1% of the dataset, the
 367 value of *Var* is $\sim 0.50 \text{ m}^2$ for three depth classes (Classes 1, 3, and 4, 64% of the data
 368 points), $\sim 0.70 \text{ m}^2$ (Class 2, 27% of the data points), and $\sim 1.12 \text{ m}^2$ (Class 5, 9% of the
 369 data points) (Table 2). It is reasonable to assume that if outliers were removed and
 370 morphological variations neglected (inherent in nearshore dynamics for a 2-year
 371 period), the algorithm would be capable of retrieving depths within $\pm 0.5 \text{ m}$ of values
 372 acquired with LiDAR data for depths between 0 and 8 m. For the five shallowest depth
 373 classes (i.e., disregarding Class 6), the value of *RMSE* ranges between 0.71 m (Class 3)
 374 and 1.10 m (Class 5), with a mean of 0.80 m.

375

376 4.2. Nearshore satellite-derived map

377 Fig. 5D, which masks data differences of $< \pm 0.5 \text{ m}$, shows that significant differences
 378 occur in the areas between profiles P1 and P2 and between P10 and P12, with the latter
 379 profiles being located in the area adjacent to the naturally migrating Ancão Inlet. The
 380 *Bias* and *DifMedian* for AoI1 are 0.01 m and 0.03 m, respectively, whereas *Var* and
 381 *RMSE* are 0.56 m^2 and 0.75 m, respectively. For AoI2, the differences are not
 382 concentrated in particular parts but are distributed over the entire area in the deeper

383 nearshore section (Fig. 8D). This behaviour was expected after analysing the spatial
384 distribution of residuals in sector E in Fig. 3, where a reduction in the number of
385 LiDAR data acquired for depths greater than 6 m can be observed. However, an
386 exception to this, where LiDAR data for depths greater than 6 m were effectively
387 acquired, includes the easternmost area of Tavira Island, adjacent to Tavira Inlet, that is,
388 AoI2. For AoI2, the *Bias* and *DifMedian* are -0.69 m and -0.63 m, whereas *Var* and
389 *RMSE* are 0.90 m² and 1.17 m, respectively (Table 3).

390 The DMM grid generated for AoI2 (Fig. 8) reveals large areas where the SDB depths
391 are shallower than the corresponding LiDAR depths, especially for depths greater than
392 6 m, which was not observed in the analysis of AoI1. This can be seen for all nine
393 cross-shore profiles extracted for AoI2 (Fig. 9), in which the maximum SDB depths are
394 close to 6 m, limiting the vectorisation of the SDB 8-m isobath (Fig. 10D). Inspection of
395 the extracted nearshore profiles in both AoI1 (Fig. 6) and AoI2 (Fig. 9) reveals that the
396 maximum deviation of the SDB in comparison with LiDAR data occurs between depths
397 of 0 and 2 m (Table 2) and that variability in the depth range of 2 to 8 m is generally
398 less than ± 0.5 m. Regarding AoI1 (Fig. 6), two profiles (P1 and P11) show quite
399 different behaviour between the SDB and both LiDAR (2- and 30-m resolution)
400 extracted profiles. All the other profiles show the expected higher elevation differences
401 between depths of 0 and 4 m, which are likely related to real morphological changes.
402 This assumption seems to be confirmed by the close match between SDB extracted
403 profiles and the LiDAR profiles for depths between 4 and 10 m. For AoI2, the
404 agreement between SDB and both LiDAR extracted profiles is significantly better for
405 depths from 0 to 6 m; however, the SDB profiles deviate significantly for the nearshore
406 profile sections at depths greater than 6 m. As LiDAR data exist for depths greater than
407 6 m, the discordance appears to be related to the optical properties of the water and/or
408 bottom properties that interfere directly with the retrieval of depth using the linear
409 algorithm (i.e., a constant and/or incorrect DN on one or more Landsat 8 bands).

410 The 2-, 4-, 6-, and 8-m isobaths from the SDB extracted for both AoI1 (Fig. 7) and AoI2
411 (Fig. 10) were compared with their equivalent LiDAR (2- and 30-m resolution) isobaths
412 and show a very consistent spatial behaviour. Major differences can be seen in the areas
413 adjacent to tidal inlets for the 2-m (Fig. 7A) and 4-m (Fig. 7B) isobaths in AoI1, as well
414 as for the 6-m isobath immediately downdrift of Tavira Inlet (Fig. 10C), and for the 8-m

415 isobath (Fig. 10D) of AoI2. It was not possible to vectorise the 8-m isobath of AoI2
416 given the limitation on retrieving bathymetry for depths greater than 6 m in AoI2.

417

418 **4.3. Validation of the depth-retrieval algorithm**

419 The reliability of the depth-retrieval algorithm to produce SDB maps was assessed
420 using a third independent data source, that is, dedicated small-scale echo-sounder
421 bathymetries acquired in AoI3 and AoI4 (Fig. 5). SDB maps were produced using the
422 determined coefficients (Eq. 6) on a new Landsat 8 scene (26 April 2013, Table 1).
423 Given the similar timings of the surveys and the satellite image, in this comparison it is
424 possible to assume negligible bathymetric change between the surveys and the date of
425 the image. Because the same areas (AoI3 and AoI4) were surveyed and the XYZ data
426 were interpolated using the same limits, method, and intervals, the DMM grid is (Figs
427 11C and 12C) used to compare the echo-sounding + RTK–DGPS map with the SDB
428 map is expected to be a reliable indicator of the SDB method for retrieving shallow-
429 water bathymetry. It also permits a direct comparison to be made of the SDB map with
430 the results of conventional hydrographic methods, both geospatially and statistically,
431 further allowing an assessment of the validity of using SDB maps for monitoring the
432 dynamics of coastal sectors. In addition, a comparison of the LiDAR bathymetry and
433 the echo-sounder data for AoI3 and AoI4 is provided in Figs 11D and 12D,
434 respectively, to illustrate the degree of temporal change within a 2-year interval (i.e.,
435 LiDAR 06/2011 and echo-sounding 04/2013). Volumetric computations showing
436 accretion/erosion morphodynamic variability are given in Table 3.

437 Figs 11C and 12C show the DMM grids between the echo-sounding + RTK–DGPS and
438 the SDB maps for AoI3 and AoI4, respectively. The DMM grids are useful for locating
439 the higher deviations and for identifying possible reasons for such deviations. Most of
440 the differences occur in areas with depths of 0–2 m (Fig. 11C) or with depths of >8 m
441 (Fig. 12C). In general, differences only rarely exceed ± 1 m, and there are extensive
442 areas with depths of 4–6 m where differences are less than ± 0.25 m. The SDB maps
443 (Figs 11B and 12B) are effective for representing the nearshore isobaths as well as the
444 shapes of the bottom morphologies. The contour limits of the swash bar (Fig. 11B) and
445 of the ebb delta (Fig 12B), both identified on the SDB maps, are clearly defined (as
446 shown by the deflection of isobaths) when compared with the echo-sounding + RTK–

447 DGPS surveys (Figs 11A and 12A, respectively). This result is relevant because both
448 surveys cover areas of complex environments: AoI3 is an area adjacent to a migrating
449 inlet and AoI4 is situated in the vicinity of a stabilised inlet (Fig. 1). The results of the
450 statistical analysis (Table 3) for AoI3 and AoI4 are similar: *Bias* is 0.01 m, *Var* is
451 0.38–0.39, and both values of *RMSE* are 0.62 m, with *DifMedian* being the only
452 parameter presenting a non-negligible difference (0.18 m and –0.07 m, respectively).
453 Finally, Figs 11D and 12D present DMM grids to assess the degree of morphological
454 change between the LiDAR and the SDB maps, given the time difference between the
455 datasets (i.e., 2 years). The red/blue values in Figs 11D and 12D signify that
456 accretion/erosion has occurred, respectively.

457 AoI3 is located adjacent to a migrating inlet (Ancão Inlet), and significant changes are
458 likely to occur during a 2-year interval (the inlet migrates from west to east, with the
459 direction of net alongshore transport being related to prevailing southwesterly
460 conditions) (Fig. 11D). Such changes include accretion in the west while the barrier
461 builds up over the former channel, forcing channel migration eastwards and causing
462 erosion of the eastern adjacent barrier (the westernmost part of Barreta Island, Fig. 1).
463 Those patterns are clearly observed in Fig. 11D with the formation of the swash bar
464 updrift (red areas), the formation of two consecutive channels in the area located in the
465 centre of the image, and general erosion in the shallow area between 0 and 2 m depth
466 (blue areas). The total surveyed area recorded erosion of $\sim 0.66 \text{ m}^3/\text{m}^2$ for the 2-year
467 period (Table 3).

468 In AoI4, accretion is observed in the central area (inlet channel) and erosion in the
469 western part of the survey area (where the ebb tidal delta is located). These observations
470 are consistent with the recent evolution of the system, that is, the ebb delta is regularly
471 dredged to counteract the sediment movement from the ebb delta towards the entrance
472 channel through the delta terminal lobe. Overall, the total surveyed area recorded
473 accretion of $\sim 0.14 \text{ m}^3/\text{m}^2$ (Table 3) for the 2-year period, which is in agreement with the
474 siltation tendency of this particular inlet, especially at the entrance channel. Excluding
475 the ebb delta and the main channel, the elevation differences only rarely exceed ± 1 m,
476 with extensive areas where differences are less than ± 0.25 m (Fig. 12D).

477

478

479 5. Discussion

480 Here, the determination of nearshore bathymetry, shoreline position, and accurate
481 nearshore isobaths for different cases were examined by comparing SDB maps with
482 data from different topographic/bathymetric surveying techniques (high- and medium-
483 resolution LiDAR and RTK-DGPS + single-beam echo-sounder bathymetries).
484 Bathymetric maps are conventionally represented by isobaths, which connect points of
485 equal depth. The inner and offshore limits of several morphological features such as
486 sand bars, deltas, and inlet channels can be both identified and spatially defined based
487 on the configuration (including deflection) of isobath contours. The delineation of these
488 morphological features is essential for performing volume computations and for
489 estimating sediment paths and budgets within coastal cells. SDB nearshore profiles and
490 isobaths retrieved for the selected areas of interest showed a very robust comparison
491 with analogue determinations using both high- and medium-resolution LiDAR datasets.
492 Discrepancies between SDB profiles and isobaths and LiDAR observations were
493 noticeable only where prominent intertidal bars occur close to the inlets, as these are the
494 areas where the most relevant morphological changes occur. It is also in these areas that
495 the depth-retrieval algorithm records the worst results because the accuracy of the depth
496 retrieval is limited by water turbidity caused by wave action, suspended sediment, and
497 particulate matter, which limit the penetration of light (i.e., from both LiDAR and OLI
498 sensors).

499 After assessing and calibrating the linear transform model, the coefficients of Eq. 6
500 were successfully used to derive SDB maps from another Landsat 8 image. Those maps
501 were compared with independent bathymetric data acquired within the same time
502 interval as the Landsat 8 image. The results presented confirmed the ability to use SDB
503 maps to adequately identify nearshore isobaths, resolve nearshore bars, extract the
504 nearshore profile, and delineate morphological features for areas with depths of <12 m
505 in shallow coastal waters without significant wave breaking. The lower accuracy and
506 precision of the SDB technique is considered to be related to the poor performance of
507 the depth-retrieval linear algorithm for depths greater than 8 m. A possible explanation
508 for this may be related to geographic and environmental controls, that is, the W and E
509 sectors are exposed to different wave regimes, causing differences in optical conditions
510 of the water (e.g., particles in suspension, chlorophyll-a, and bottom properties). Where

511 the depth-retrieval linear algorithm is successful in extracting depths, the extracted
512 values present higher residuals (areas adjacent to Tavira Inlet, Fig. 3 Class 5).

513 In this paper, a DOS method was applied to perform the atmospheric correction and a
514 linear retrieval algorithm was applied using coefficients computed from a multiple
515 linear regression performed with high-resolution LiDAR data. The adopted procedures
516 are straightforward and are based on freely available images, and allowed shallow
517 nearshore bathymetry to be represented well for depths less than 12 m. However, to
518 improve the stability or robustness of the regressed model parameters over time, other
519 Landsat 8 satellite images need to be analysed and compared with nearshore surveys. As
520 an example, Brando et al. (2009) compared the accuracy of the depth-retrieval algorithm
521 by comparison with acoustic depths at Rous Channel located in Moreton Bay
522 (Australia) for depths of 0–30 m, with a 2-month interval between datasets. A greater
523 agreement was found in shallow, clear water than in deeper or more turbid water near
524 the coast (e.g., from 1–5 m depth, *Bias* of 0.43 m, *DifMedian* of 0.42 m, and *RMSE* of
525 1.35 m). Brando et al. (2009) optimised the inversion algorithm by comparing the
526 measurable remote sensing reflectance from the image with a modelled reflectance. The
527 procedure adopted by Brando et al. (2009) allowed differences related to environmental
528 variables such as water column depth, substrate composition, and the concentration of
529 optical active constituents on the water column (chlorophyll-a, the concentration of
530 dissolved organic matter, and non-algal particles) to be minimised, as well the range of
531 the technique to be extended.

532 In general, SDB retrieved from Landsat 8 images presents a new perspective for
533 remotely sensed bathymetry extraction and can be used to complement data from survey
534 sources such as single-beam echo-sounder data, which are normally obtained at medium
535 (profiling interval 25–30 m) to coarse (>30 m) resolution. This implies that SDB can
536 effectively deliver data to complement such surveys and provide a similar spatial
537 representation of nearshore variability. In particular, the ability to extract depth contours
538 from satellite-derived bathymetry can be a straightforward and accessible method for
539 evaluating morphological changes in the nearshore. This method has high potential for
540 acquiring cost-effective, long-term time-series of coastal morphology over extensive
541 areas and at the same time provides high-frequency data (i.e., approximately fortnightly
542 intervals, 16 days). The medium-resolution maps derived from the presented method
543 can be used to improve the prediction of hydro-morphodynamic modelling simulations

544 such as those given by X-Beach (Roelvink et al., 2009) by allowing the continuous
545 extraction of model input morphodynamic parameters (e.g., submerged beach slope).

546

547 **6. Conclusion**

548 An improved understanding of coastal zone evolution and processes is based partially
549 on the existence of detailed and reasonably accurate monitoring datasets. Such datasets
550 have become fundamental for coastal research, modelling, and management. The
551 present contribution assessed the potential of satellite-derived bathymetry (SDB) maps
552 for providing nearshore bathymetry at medium resolution from freely available Landsat
553 8 imagery, and revealed the value of the approach for the monitoring and management
554 of coastal morphological evolution. The results showed that bathymetry obtained from
555 multi-spectral satellite data is more accurate for shallow water depths (0 to 8 m) than for
556 greater depths (8–12 m), a limitation inherent in a passive optical detection system;
557 however, in the Ria Formosa case study, the decrease in accuracy with depth was also a
558 function of the more limited availability of the LiDAR data used to tune the image-to-
559 depth conversion algorithm at greater depths. The SDB maps were able to provide good
560 approximations of the shoreline position and nearshore isobath contours for different
561 cases along a highly complex coastline that includes morphological features such as
562 barrier islands, inlets, ebb deltas, and alongshore and swash bars. In all instances, the
563 extracted morphological features (i.e., nearshore isobaths and profiles) displayed
564 reasonable accuracy when compared with those derived from traditional monitoring
565 methods.

566 Improved satellite imagery collection, processing algorithms, and workflows make SDB
567 a real and useful survey solution for monitoring coastal areas and for producing rapidly
568 deliverable digital bathymetric models. Although SDB has great potential in its current
569 state, the good quality of the results presented here for the 60-km stretch of coast of the
570 Ria Formosa area is inherently related to the availability of the high-frequency LiDAR
571 data that were used to perform the regression to obtain the coefficients of Lyzenga's
572 (1978, 1985) model. In other words, if no in situ water depths are available and/or depth
573 measurements are sparse, then the model cannot be applied with the same degree of
574 rigor. However, SDB has the potential to complement traditional but expensive
575 maritime charting techniques such as acoustic and LiDAR surveys, because the method

576 does not need devoted boats, aircraft, or other survey systems. Depending on weather
577 conditions and satellite orbit timings, the surveys can be performed on a regular basis,
578 giving the potential to create historical datasets from imaging archives. If the robustness
579 of the coefficients is further analysed, the technique can be used to derive nearshore
580 bathymetric maps to assist with coastal monitoring. Finally, the accuracy of SDB maps
581 is partly a function of water clarity, depth, and wave climate. Better approximations
582 could be derived by using algorithms that correct for environmental variables such as
583 the concentration of optically active constituents in the water column (e.g., chlorophyll-
584 a, organic dissolved matter, and suspended sediment). With respect to wave climate, the
585 method presented here works better for calm conditions, and major deviations in the
586 accuracy of depth assessments occur in the breaking zone.

587

588 **Acknowledgments**

589 André Pacheco and Carlos Loureiro were supported by the Portuguese Foundation for
590 Science and Technology (grant numbers SFRH/BPD/76110/2011 and
591 SFRH/BPD/85335/2012). AoI3 bathymetric data were acquired under project RUSH
592 (from RUn up to overwaSH) (PTDC/CTE-GIX/116814/2010) funded by the Portuguese
593 Foundation for Science and Technology. The authors acknowledge the anonymous
594 reviewers, whose comments helped to greatly improve an earlier version of this
595 manuscript.

596

597 **List of Acronyms**

598	AoI	Area of Interest
599	DEM	Digital Elevation Model
600	DMM	Difference Map Method
601	DOS	Dark Subtraction Object
602	LiDAR	Light Detecting and Ranging
603	NIR	Near Infrared Band
604	OLI	Operational Land Imagery
605	SDB	Satellite-Derived Bathymetry

606	SNR	Signal to Noise Ratio
607	TIRS	Thermal Infrared Sensor
608		
609	List of Symbols	
610	$a(\lambda)$	Absorption coefficient
611	$b_b(\lambda)$	Backscatter coefficient
612	d_b	Bottom depth
613	DN	Digital number
614	d	Earth–Sun distance
615	E_d	Downwelling irradiance
616	E_o	Solar constant
617	$E_{sum\lambda_i}$	Exo-atmospheric solar irradiance from band λ_i
618	H_s	Significant wave height
619	θ_0	Solar zenith angle
620	θ_v	Sub-surface viewing angle from nadir
621	θ_w	Sub-surface solar zenith angle
622	L_T	Total radiance (measured by the satellite)
623	L_w	Water-leaving radiance
624	$L_{1\%}$	Minimum scatter radiance
625	R	Irradiance reflectance
626	R_b	Bottom albedo
627	R_r	Rayleigh reflectance
628	R_{rs}	Remote sensing reflectance
629	R_T	Total reflectance
630	R_w	Reflectance of water
631	R_∞	Water reflectance (if optically deep)

632	TOA	Top of Atmosphere Reflectance
633	T_0	Transmission coefficient Sun-to-Earth
634	T_1	Transmission coefficient Earth-to-Sun
635	Z_{LiDAR}	Depth acquired with LiDAR
636	Z_{LSAT8}	Satellite-derived depth
637	φ	Viewing azimuth angle from solar plane

638

639 **References**

- 640 Albert, A., Gege, P., 2006. Inversion of irradiance and remote sensing reflectance in
641 shallow water between 400 and 800 nm for calculation of water and bottom
642 properties. *Applied Optics* 45: 2331–2343.
- 643 Albert, A., Mobley, C.D., 2003. An analytical model for subsurface irradiance and
644 remote sensing reflectance in deep and shallow case-2 waters. *Opt. Express* 11:
645 2873–2890.
- 646 Brando, V., Anstee, J.M., Wettle, M., Dekker, A.G., Phinn, S.R., Roelsema, C., 2009. A
647 physical based retrieval and quality assessment of bathymetry from suboptimal
648 hyperspectral data. *Remote Sens. Environ.* 113: 755–790.
- 649 Chavez, P.S., Jr. 1988. An improved dark-object subtraction technique for atmospheric
650 scattering correction of multispectral data. *Remote Sens. Environ.* 24: 459–479.
- 651 Chavez, P.S., Jr. 1996. Image-based atmospheric corrections—revisited and improved.
652 *Photogramm. Eng. Remote Sensing* 62(9): 1025–1036.
- 653 Costa M., Silva R., Vitorino J., 2001. Contribuição para o estudo do clima de agitação
654 marítima na costa Portuguesa. 2as Jornadas Portuguesas de Engenharia Costeira e
655 Portuária in CD-ROM. (in Portuguese).
- 656 Dekker A.G., Phinn, S.R., Anstee J., Bissett, P., Brando V., Casey, B., Fearn, P.,
657 Hedley, J., Klonowski, W., Lee, Z.P., Lynch, M., Lyons, M., Mobley, C.,
658 Roelsema, C. 2011. Intercomparison of shallow water bathymetry, hydro-optics,
659 and benthos mapping techniques in Australian and Caribbean coastal
660 environments. *Limnol. Oceanogr. Methods* 9: 396–425.

- 661 Hicks D.M., Hume T.M., 1997. Determining sand volumes and bathymetric change on
662 an ebb-tidal delta. *J. Coast. Res.* 13 (2): 407–416.
- 663 Horta, J., Pacheco, A., Moura, D., Ferreira, Ó., 2014. Can recreational Echosounder-
664 Chartplotter systems be used to perform accurate nearshore bathymetric surveys?
665 *Ocean Dyn.* 64:1555–1567.
- 666 IHO, 2008. International Hydrographic Organization Standards S-44 for Hydrographic
667 Surveys, Special Publication No 44, 28 pp.
- 668 Keith, D.J., Shaeffer, B.A., Lunetta, R.S., Gould, R.W., Rocha, K., Cobb, D.J. 2014.
669 Remote sensing of selected water-quality indicators with the hyperspectral imager
670 for the coastal ocean (HICO) sensor. *Int. J. Remote Sens.* 35(9): 2927–2962.
- 671 Lyzenga, D.R. 1978. Passive remote sensing techniques for mapping water depth and
672 bottom features. *Appl. Opt.* 17: 379–383.
- 673 Lyzenga, D.R. 1985. Shallow-water bathymetry using combined LiDAR and passive
674 multispectral scanner data. *Int. J. Remote Sens.* 6: 115–125.
- 675 Mobley, C.D., Sundman L.K., Davis, C.O., Downes, T.V., Leathers, R.A, Montes
676 M.J., Bissett W.P., Kohler D.D., Reid R.P., Louchard E.M., Gleason A., 2005.
677 Interpretation of hyperspectral remote-sensing imagery via spectrum matching
678 and look-up tables. *Appl. Opt.* 44:3576–3592.
- 679 Nazeer, M., Nichols, J.E., Yung, Y. 2014. Evaluation of atmospheric correction models
680 and Landsat surface reflectance product in an urban coastal environment. *Int. J.*
681 *Remote Sens.* 35(16): 6671–6291.
- 682 Pacheco, A., Williams, J.J., Ferreira, Ó., Garel, E., Reynolds, S., 2011. Application of
683 Sediment Transport Models to a Multiple-Inlet System. *Estuar. Coast. Shelf Sci.*
684 95: 119–134.
- 685 Pawlowicz, R., Beardsley, B., Lentz, S., 2002. Classical tidal harmonic analysis
686 including error estimates in MATLAB using T_TIDE. *Comput. Geosci.* 28: 929–
687 937.
- 688 Roelvink, D., Reniers, A., van Dongerenb, A., de Vries, J., McCall, R., Lescinski, J.,
689 2009. Modelling storm impacts on beaches, dunes and barrier islands. *Coastal*
690 *Eng.* 56(11–12): 1133–1152.

- 691 Roy, D.P., Wulder, M.A., Loveland, T.R., Woodcock, C.E., Allen, R.G., Anderson,
692 M.C., Helder, D., Irons, J.R., Johnson, D.M., Kennedy, R., Scambos, T.A.,
693 Schaaf, C.B., Schott, J.R., Sheng, Y., Vermote, E.F., Belward, A.S., Bindschadler,
694 R., Cohen, W.B., Gao, F., Hipple, J.D., Hostert, P., Huntington, J., Justice, C.O.,
695 Kilic, A., Kovalsky, V., Lee, Z.P., Lymburner, L., Masek, J.G., McCorkel, J.,
696 Shuai, Y., Trezza, R., Vogelmann, J., Wynne, R.H., Zhu, Z. 2014. Landsat-8:
697 Science and product vision for terrestrial global change research. *Remote Sens.*
698 *Environ.*145: 154–172.
- 699 Stauble D. 1998. Techniques for measuring and analysing inlet ebb shoal evolution.
700 *Coast. Eng. Techn. Note* IV(13), 12 pp.
- 701 Stumpf, R.P., Holderied, K., Sinclair, M., 2003. Determination of water depth with high
702 resolution satellite imagery over variable bottom types. *Limnol. Oceanogr.* 48 (I/
703 2): 547–556.

DRAFT

704 **Table Captions**

705 **Table 1.** Details of the datasets used in the present study (LiDAR, Landsat 8 scenes, and echo-sounder +
706 RTK–DGPS). XY is referenced to WGS84 UTM ZONE 29 and Z to mean sea level (MSL).

707 **Table 2.** Constant coefficients derived from the multiple linear regression between water reflectance band
708 and LiDAR depth. Residual statistics between the satellite-derived depth (Z_{LSat8}) and (Z_{Li}) and LiDAR
709 depth for different depth classes.

710 **Table 3.** AoI1 univariate statistics obtained by comparing Bm2 and Bm3. AoI2 univariate statistics
711 obtained by comparing Bm2 and Bm3. AoI3 and AoI4 univariate statistics obtained by comparing the
712 echo-sounding + RTK–DGPS survey performed in late April 2013 with the SDB maps produced using
713 the Landsat 8 scene from 26 April 2013.

714

715 **Figure Captions**

716 **Figure 1.** (A) Ria Formosa multi-inlet system (southern Portugal). Areas of Interest AoI1 and AoI3 (B)
717 and AoI2 and AoI4 (C) are represented by aerial photography images to a depth limit of ~12 m.

718 **Figure 2.** Workflow processing steps for deriving SDB maps from Landsat 8 images (DN: Digital
719 number; L_T : Total radiance; $L_{1\%}$: Minimum scatter radiance; R_w : Reflectance of water; R_T : Total
720 reflectance; R_w : Water reflectance; X_i , X_j , and X_k are from Lyzenga's (1978, 1985) linear solution for
721 albedo correction; a_0 , a_i , a_j , and a_k are constants determined by multiple linear regression; Z_{LiDAR} : Depth
722 acquired with LiDAR; Z_{LSAT8} : Satellite-derived depth.

723 **Figure 3.** Spatial distribution of the residual between Z_{LSat8} and Z_{LiDAR} along X coordinate WGS84
724 UTM29 for different depth classes. Vertical grey bands represent the inlet areas. Horizontal dark-grey
725 bands represent residuals less than 2 m. The smaller amount of data at greater depths results from LiDAR
726 data limitations (see main text Section 3.2.).

727 **Figure 4.** Histogram of differences between satellite-derived depth (Z_{LSat8}) and LiDAR depth (Z_{LiDAR})
728 by depth class.

729 **Figure 5.** (A) AoI1 bathymetry contour map (Bm1) using the 2-m resolution 2011 LiDAR data
730 superimposed with an aerial photograph of AoI1. (B) Bathymetry contour map (Bm2) with a 30-m
731 resolution using 2011 LiDAR data resampling. (C) Satellite-derived bathymetry contour map (Bm3) with
732 a 30-m resolution. (D) Difference map between Bm2 and Bm3. P1 to P12 represent the locations of the
733 profiles extracted from bathymetric maps Bm1 and Bm2.

734 **Figure 6.** AoI1 nearshore cross-profiles spaced by 1000 m and extracted from bathymetric contour maps
735 Bm1, Bm2, and Bm3.

736 **Figure 7.** (A) 2-m, (B) 4-m, (C) 6-m, and (D) 8-m isobaths extracted from Bm1 (LiDAR 2 m), Bm2
737 (LiDAR 30 m), and Bm3 (SDB 30 m) for AoI1. XY coordinates are referred to WGS84 UTM29 and Z
738 contour lines to MSL.

739 **Figure 8.** (A) AoI2 bathymetry contour map (Bm1) using the 2-m resolution 2011 LiDAR data
740 superimposed with an aerial photograph of AoI2. (B) Bathymetry contour map (Bm2) with a 30-m
741 resolution using 2011 LiDAR data resampling. (C) Satellite-derived bathymetry contour map (Bm3), also
742 showing AoI3. (D) Difference map between Bm2 and Bm3. P1 to P9 represent the locations of the
743 profiles extracted from bathymetric maps Bm1, Bm2, and Bm3.

744 **Figure 9.** AoI2 nearshore cross-profiles spaced by 1000 m and extracted from bathymetric contour maps
745 Bm1, Bm2, and Bm3.

746 **Figure 10.** (A) 2-m, (B) 4-m, (C) 6-m, and (D) 8-m isobaths extracted from Bm1 (LiDAR 2m), Bm2
747 (LiDAR 30 m), and Bm3 (SDB 30 m) for AoI2. XY coordinates are referred to WGS84 UTM29 and Z
748 contour lines to MSL.

749 **Figure 11.** (A) AoI3 bathymetry contour map acquired using an echo-sounder synchronised with a RTK–
750 DGPS in the area adjacent to Ancão Inlet on 26 April 2013. (B) Satellite-derived bathymetry (SDB)
751 contour map (Bm3) with a 30-m resolution. (C) Difference map between A and B. (D) Difference map
752 between LiDAR 05/2011 and SDB data derived from the Landsat 8 image of 26 April 2013; the red/blue
753 values signify that accretion/erosion has occurred, respectively.

754 **Figure 12.** (A) AoI4 bathymetry contour map acquired using an echo-sounder synchronised with a RTK–
755 DGPS in and around Tavira Inlet on 30 April 2013. (B) Satellite-derived bathymetry (SDB) contour map
756 (Bm3) with a 30-m resolution. (C) Difference map between A and B. (D) Difference map between
757 LiDAR 05/2011 and SDB data derived from the Landsat 8 image of 26 April 2013; the red/blue values
758 signify that accretion/erosion has occurred, respectively.

759

760 **Table 1.** Details of the datasets used in the present study (LiDAR, Landsat 8 scenes, and echo-sounder +
 761 RTK–DGPS). XY is referenced to WGS84 UTM ZONE 29 and Z to mean sea level (MSL)
 762

Dataset	Details and coverage	Type/Resolution
LiDAR	Topographic LiDAR LeicaALS60 Bathymetric LiDAR HawkEyeII Coverage: Portugal, to 8–10 m depth Datum: WGS84; Ellipsoid: WGS84 UTM Zone: 29; Z referred to MSL Date acquired= 2011-05	Combined model (topographic plus bathymetric LiDAR): Resolution 2 m Order 1A International Hydrographic Organisation Standards 44 (2008)
	Scene: LC82030342013164LGN00 Map projection: UTM Datum: WGS84; Ellipsoid: WGS84 UTM Zone: 29 Coverage: X: 494400–720900 Y: 4037100–4258200 Date acquired: 2013-06-13	8 Bands Digital Numbers (DNs) each 30 m Image attributes Min/Max Radiance Min/Max Reflectance Min/Max Pixel Value Radiometric Rescaling TIRS Thermal Constants Projection Parameters
Landsat 8	Scene: LC82030342013116LGN01 Map projection: UTM Datum: WGS84; Ellipsoid: WGS84 UTM Zone: 29 Coverage: X: 494400–720900 Y: 4037100–4258200 Date acquired: 2013-04-26	All in the *.MTL file provided by United States Geological Service
Echo-Sounder + RTK–DGPS	Sounding: EchoTrac CV 100 Frequency: 200 kHz Positioning: RTK–DGPS TrimbleR6/5800 GPS Satellite signals: L1C/A, L1C, L2C, L2E, L5. Datum: WGS84; Ellipsoid: WGS84 UTM Zone: 29; Z referred to MSL Coverage: AoI3 Barreta Island AoI4 Tavira Inlet Date acquired 2013-04-26 (AoI3) 2013-04-30 (AoI4)	1 Hz data Resolution 25 m (single-beam echo-sounder lines run parallel at pre-planned line spacing); Bathymetry tide corrected (RTK) Echo-sounding accuracy: 0.01 m ±0.1% of depth Positioning performance for RTK surveying: Horizontal: 8 mm + 1 ppm RMS Vertical: 15 mm + 1 ppm RMS

763

764

765 **Table 2.** Constant coefficients derived from the multiple linear regression between water reflectance band
 766 and LiDAR depth. Residual statistics between the satellite-derived depth (Z_{LSat8}) and (Z_{Li}) and LiDAR
 767 depth for different depth classes

768

Multiple Linear Regression

$$Z_{LSat8} = a_0 + a_i(X_i) + a_j(X_j) + a_k(X_k)$$

$R^2 = 0.88$, $N = 35247$ $a_0 = -2.39$; $a_i = -6.05$; $a_j = -0.33$; $a_k = 8.25$

Residual statistics ($Z_{LSat8} - Z_{LiDAR}$)

	Depth Class (m)						
	Class 1 [0–2]	Class 2 [2–4]	Class 3 [4–6]	Class 4 [6–8]	Class 5 [8–10]	Class 6 [10–12]	Overall [0–12]
N	6145	9619	8377	7640	3258	208	35247
Bias (m)	0.61	0.01	-0.07	-0.26	-0.31	-1.16	-0.20
Std (m)	0.71	0.84	0.71	0.71	1.06	1.28	0.89
Var (m ²)	0.51	0.70	0.50	0.50	1.12	1.63	0.83
DifMedian (m)	0.60	0.05	-0.07	-0.37	-0.02	-0.77	-0.10
RMSE (m)	0.94	0.84	0.71	0.75	1.10	1.72	1.01
Max (m)	6.06	3.43	2.83	3.65	2.75	0.73	n/a
Min (m)	-2.03	-3.34	-3.72	-3.97	-3.54	-4.79	n/a

769

770

DRAFT

771 **Table 3.** AoI1 univariate statistics obtained by comparing Bm2 and Bm3. AoI2 univariate statistics
 772 obtained by comparing Bm2 and Bm3. AoI3 and AoI4 univariate statistics obtained by comparing the
 773 echo-sounding + RTK–DGPS survey performed in late April 2013 with the SDB maps produced using
 774 the Landsat 8 scene from 26 April 2013

775

AoI1	Bathymetric Contour Map	
	Bm2 (LiDAR 30 m)	Bm3 (SDB 30 m)
Mean (Z) (m)	-5.93	-5.94
Median (Z) (m)	-6.12	-6.41
Min (Z) (m)	-10.39	-10.77
Max (Z) (m)	-0.09	-0.46
Std (Z) (m)	2.62	2.84
Var (\hat{z})		0.56
Bias(\hat{z}, z)		0.01
DifMedian(\hat{z}, z)		0.03
RMSE(\hat{z})		0.75

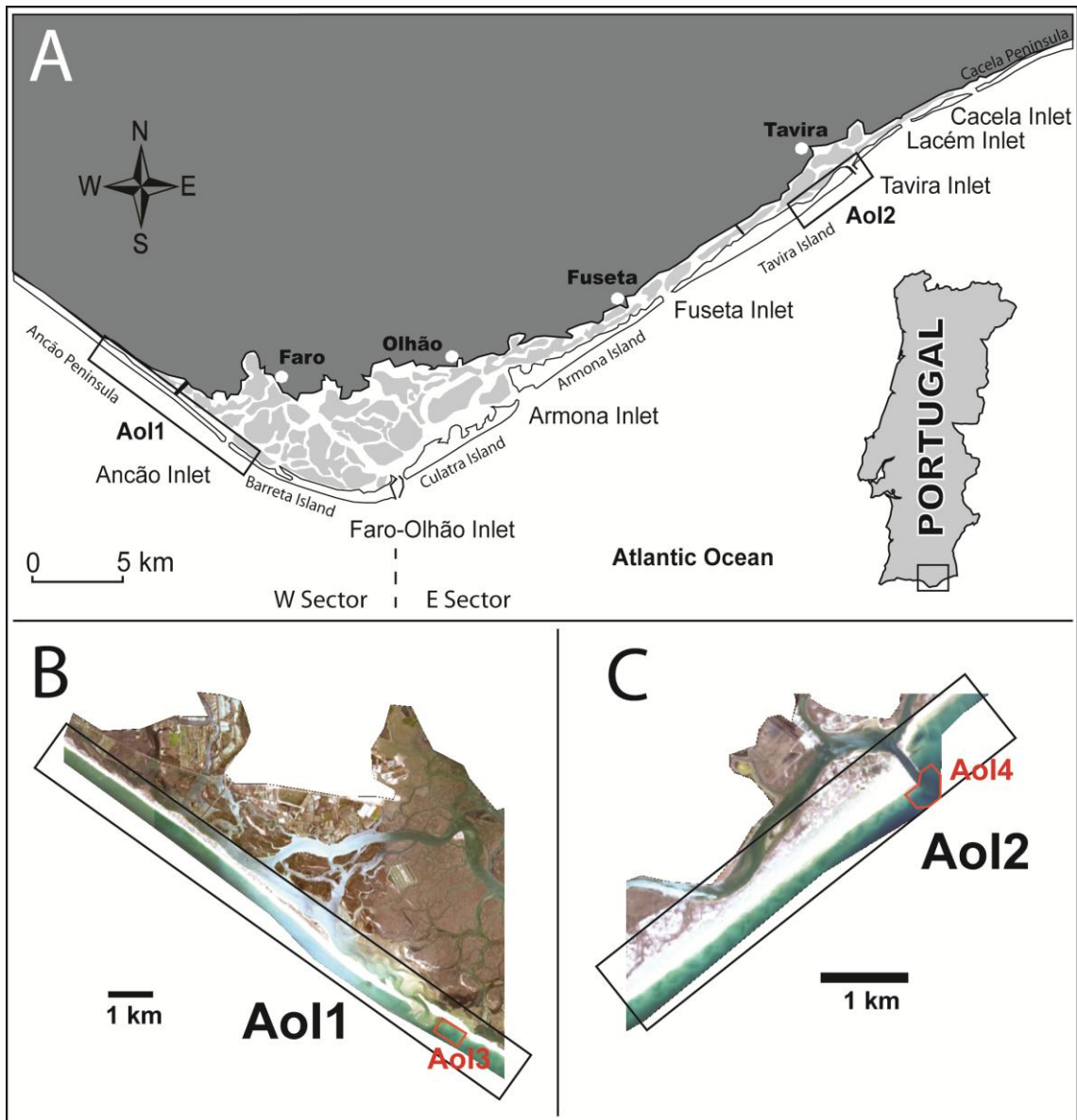
AoI2	Bathymetric Contour Map	
	Bm2 (LiDAR 30 m)	Bm3 (SDB 30 m)
Mean (Z) (m)	-5.38	-4.69
Median (Z) (m)	-6.25	-5.64
Min (Z) (m)	-10.24	-7.38
Max (Z) (m)	-0.01	-0.52
Std (Z) (m)	2.74	2.00
Var (\hat{z})		0.90
Bias(\hat{z}, z)		-0.69
DifMedian(\hat{z}, z)		-0.63
RMSE(\hat{z})		1.17

AoI3	Bathymetric Contour Map	
	Echo-Sounder + RTK–DGPS	SDB 30 m
Mean (Z) (m)	-4.43	-4.44
Median (Z) (m)	-4.42	-4.72
Min (Z) (m)	-8.32	-7.97
Max (Z) (m)	-0.68	-0.13
Std (Z) (m)	1.75	2.21
Var (\hat{z})		0.39
Bias(\hat{z}, z)		0.01
DifMedian(\hat{z}, z)		0.18
RMSE(\hat{z})		0.62

AoI4	Bathymetric Contour Map	
	Echo-Sounder + RTK–DGPS	SDB 30 m
Mean (Z) (m)	-5.75	-5.53
Median (Z) (m)	-6.23	-5.93
Min (Z) (m)	-8.67	-6.90
Max (Z) (m)	-1.67	-0.74
Std (Z) (m)	1.44	1.28
Var (\hat{z})		0.38
Bias(\hat{z}, z)		0.01
DifMedian(\hat{z}, z)		-0.07
RMSE(\hat{z})		0.62

776

777

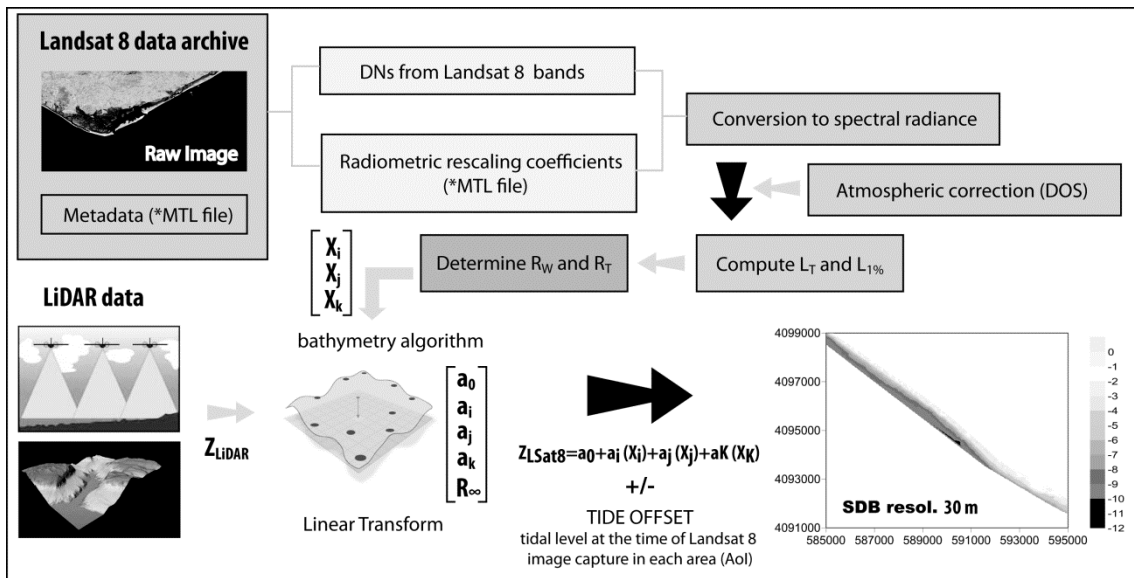


778

779 **Figure 1.** (A) Ria Formosa multi-inlet system (southern Portugal). Areas of Interest AoI1 and AoI3 (B)
 780 and AoI2 and AoI4 (C) are represented by aerial photography images to a depth limit of ~12 m.

781

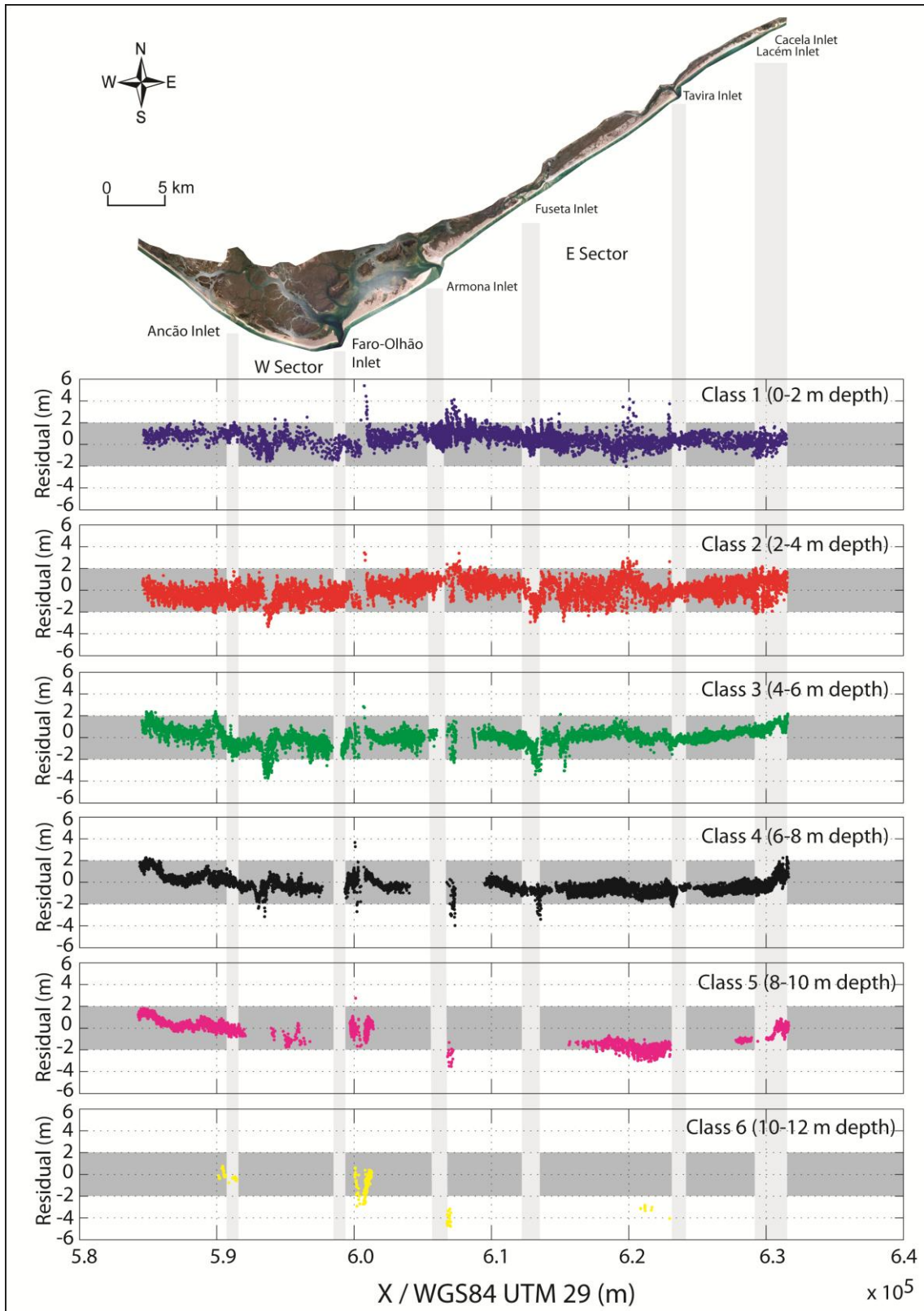
782



783

784 **Figure 2.** Workflow processing steps for deriving SDB maps from Landsat 8 images (DN: Digital
 785 number; L_T : Total radiance; $L_{1\%}$: Minimum scatter radiance; R_w : Reflectance of water; R_T : Total
 786 reflectance; R_∞ : Water reflectance; X_i , X_j , and X_k are from Lyzenga's (1978, 1985) linear solution for
 787 albedo correction; a_0 , a_i , a_j , and a_k are constants determined by multiple linear regression; Z_{LiDAR} : Depth
 788 acquired with LiDAR; Z_{LSAT8} : Satellite-derived depth.

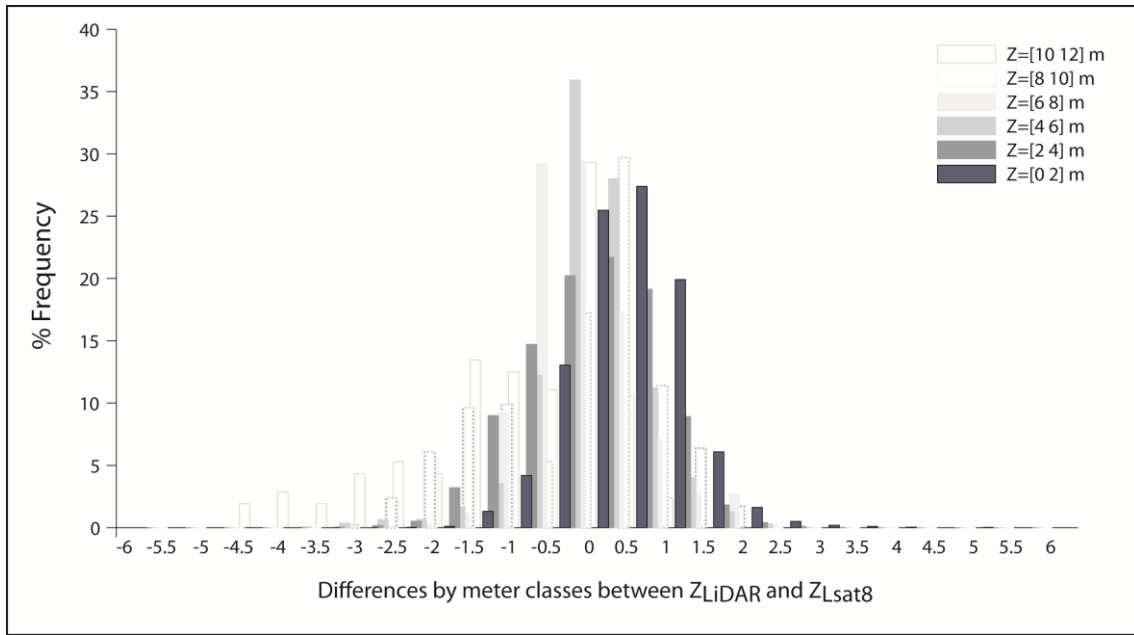
789



791

792 **Figure 3.** Spatial distribution of the residual between Z_{LSat8} and Z_{LiDAR} along X coordinate WGS84
 793 UTM29 for different depth classes. Vertical grey bands represent the inlet areas. Horizontal dark-grey
 794 bands represent residuals less than 2 m. The smaller amount of data at greater depths results from LiDAR
 795 data limitations (see main text Section 3.2.).

796



797

798

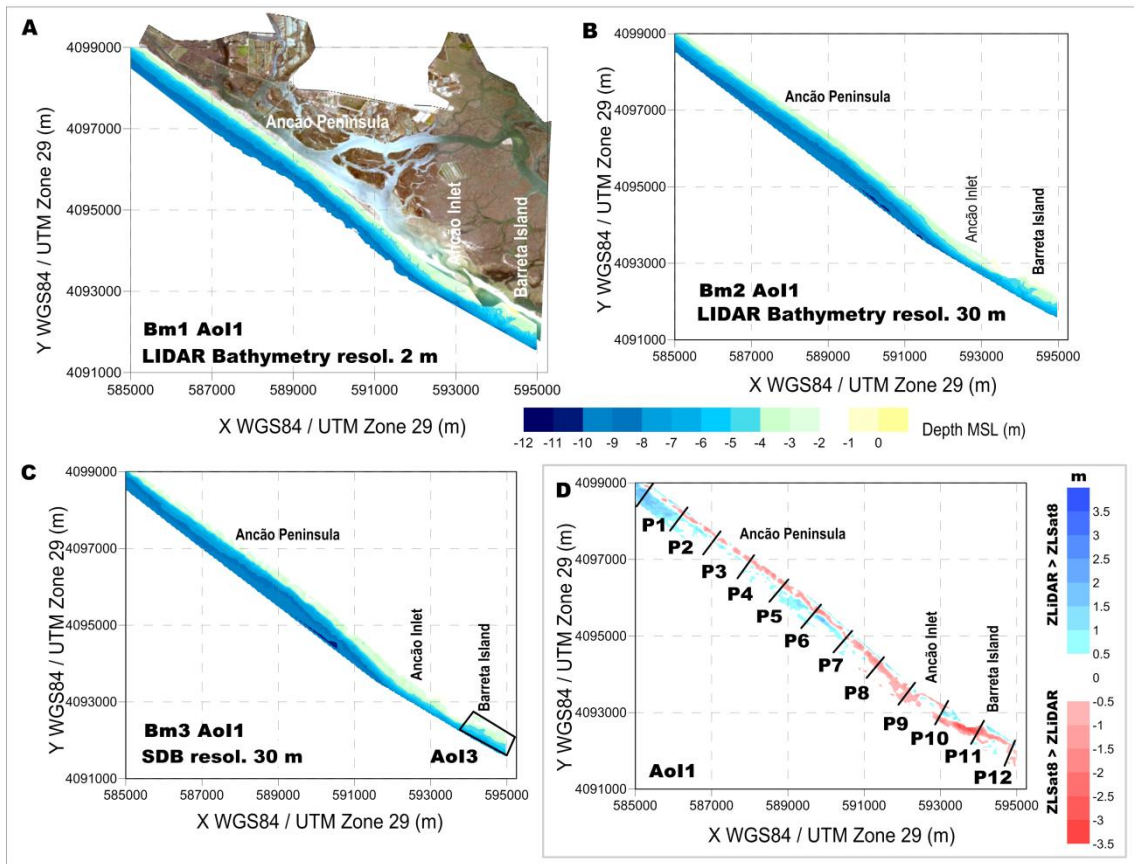
799

800

Figure 4. Histogram of differences between satellite-derived depth (Z_{Lsat8}) and LiDAR depth (Z_{LiDAR}) by depth class.

DRAFT

801

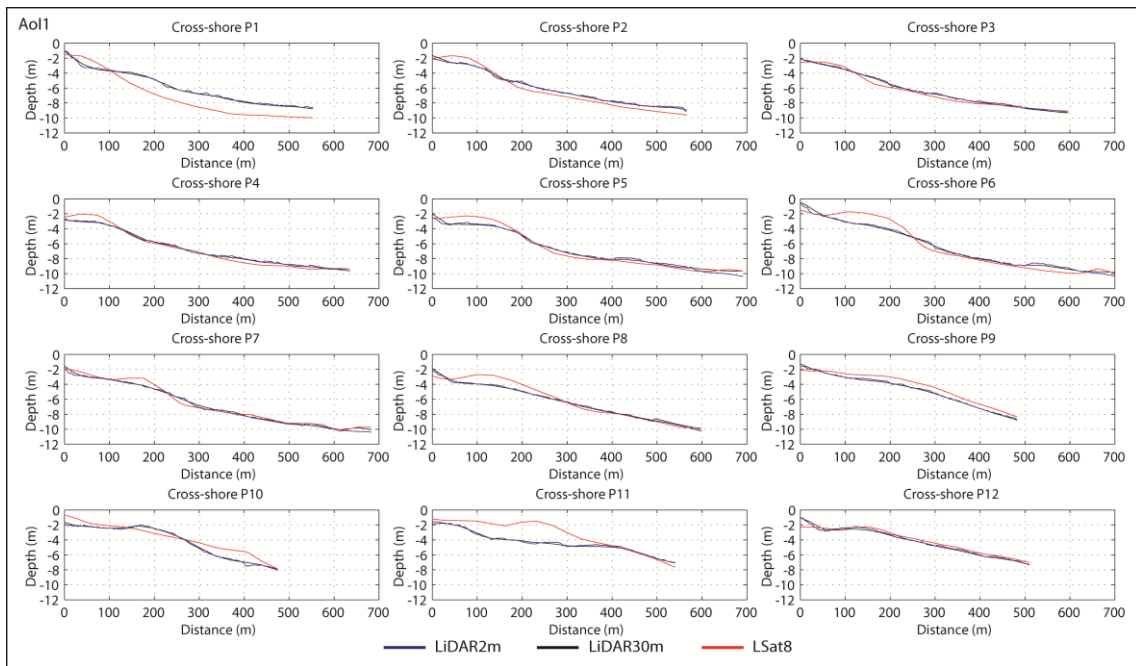


802

803 **Figure 5.** (A) AoI1 bathymetry contour map (Bm1) using the 2-m resolution 2011 LiDAR data
 804 data superimposed with an aerial photograph of AoI1. (B) Bathymetry contour map (Bm2) with a 30-m
 805 resolution using 2011 LiDAR data resampling. (C) Satellite-derived bathymetry contour map (Bm3) with
 806 a 30-m resolution. (D) Difference map between Bm2 and Bm3. P1 to P12 represent the locations of the
 807 profiles extracted from bathymetric maps Bm1 and Bm2.

808

809

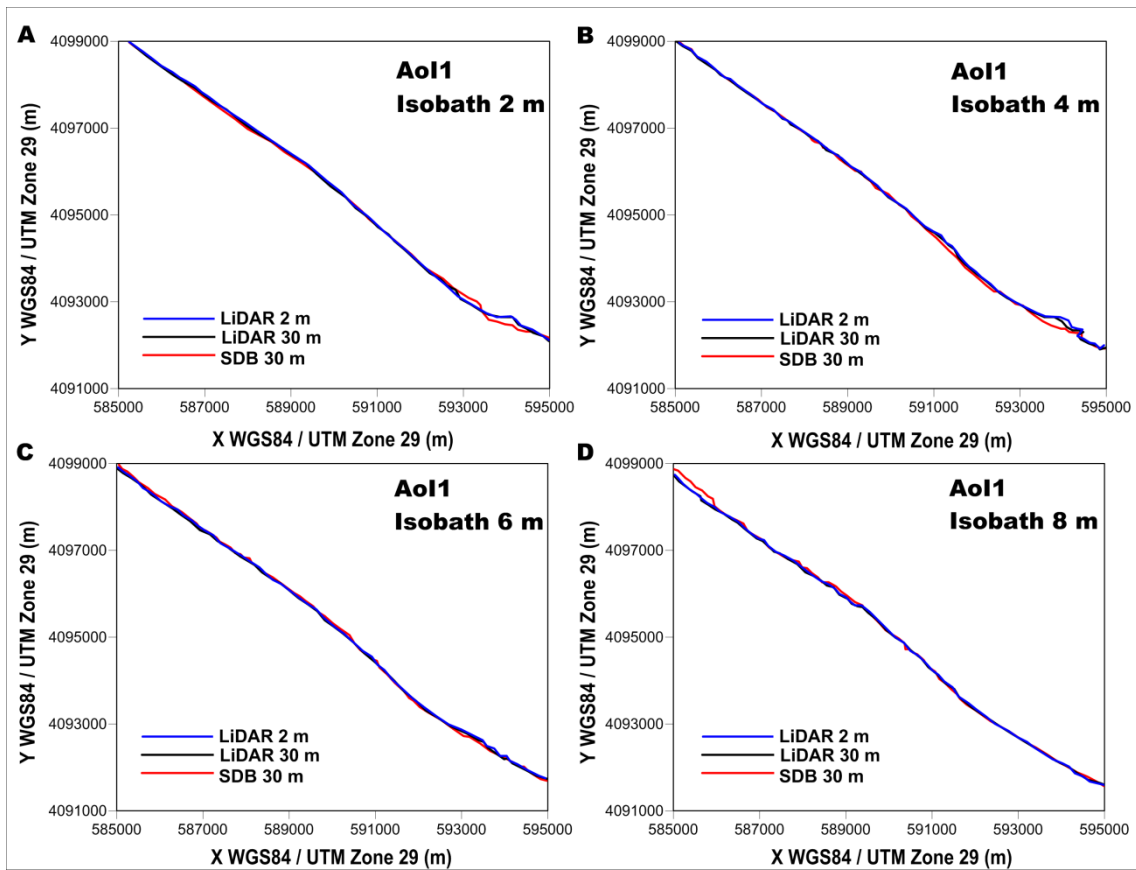


810

811 **Figure 6.** AoI1 nearshore cross-profiles spaced by 1000 m and extracted from bathymetric contour maps
812 Bm1, Bm2, and Bm3.

813

814

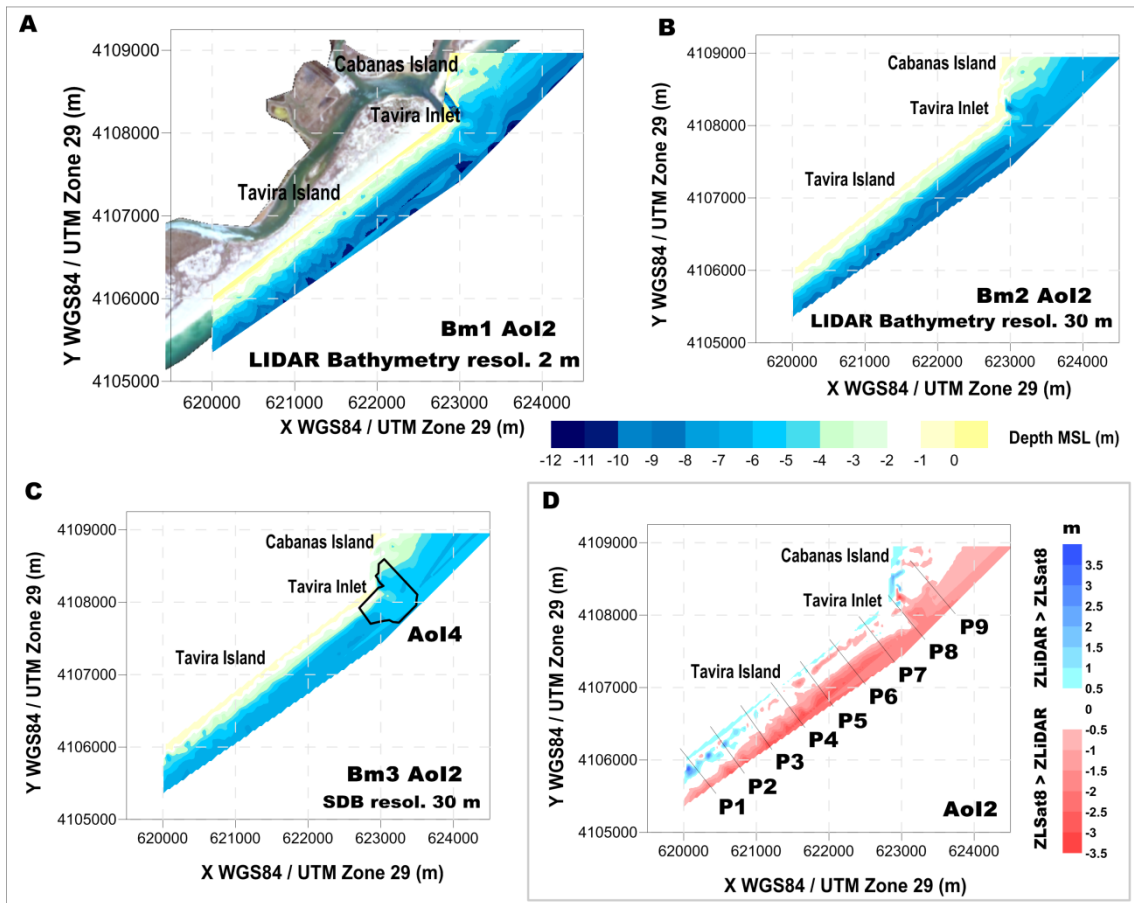


815

816 **Figure 7.** (A) 2-m, (B) 4-m, (C) 6-m, and (D) 8-m isobaths extracted from Bm1 (LiDAR 2 m), Bm2
 817 (LiDAR 30 m), and Bm3 (SDB 30 m) for Aol1. XY coordinates are referred to WGS84 UTM29 and Z
 818 contour lines to MSL.

819

820

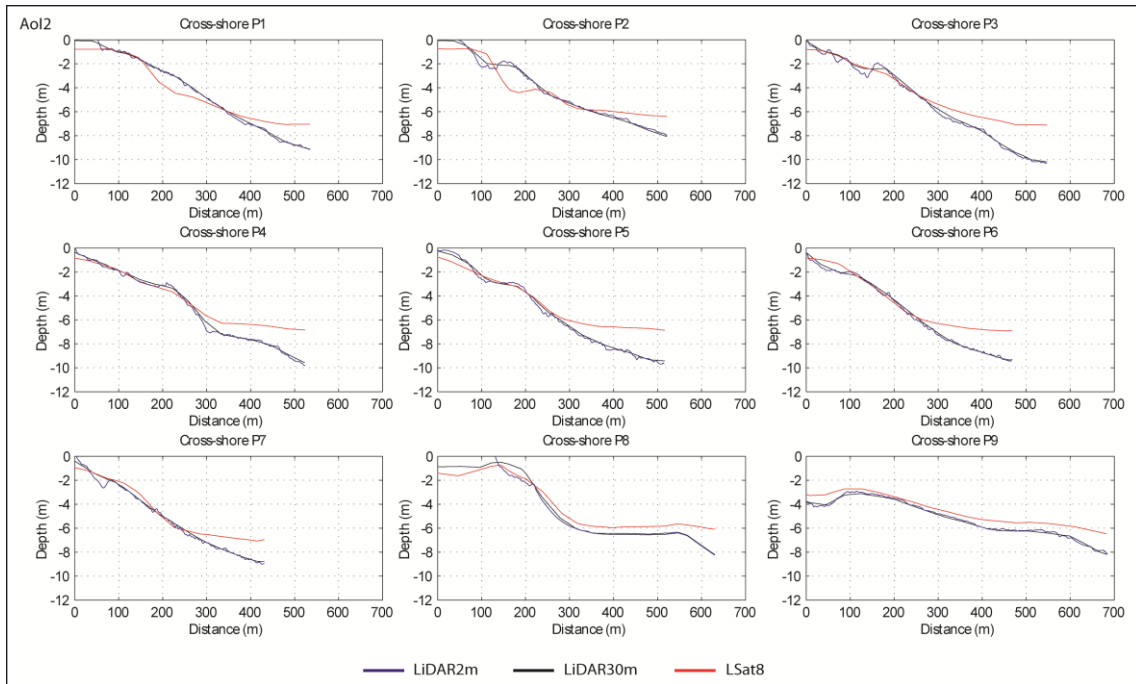


821

822 **Figure 8.** (A) AoI2 bathymetry contour map (Bm1) using the 2-m resolution 2011 LiDAR data
 823 superimposed with an aerial photograph of AoI2. (B) Bathymetry contour map (Bm2) with a 30-m
 824 resolution using 2011 LiDAR data resampling. (C) Satellite-derived bathymetry contour map (Bm3), also
 825 showing AoI3. (D) Difference map between Bm2 and Bm3. P1 to P9 represent the locations of the
 826 profiles extracted from bathymetric maps Bm1, Bm2, and Bm3.

827

828



829

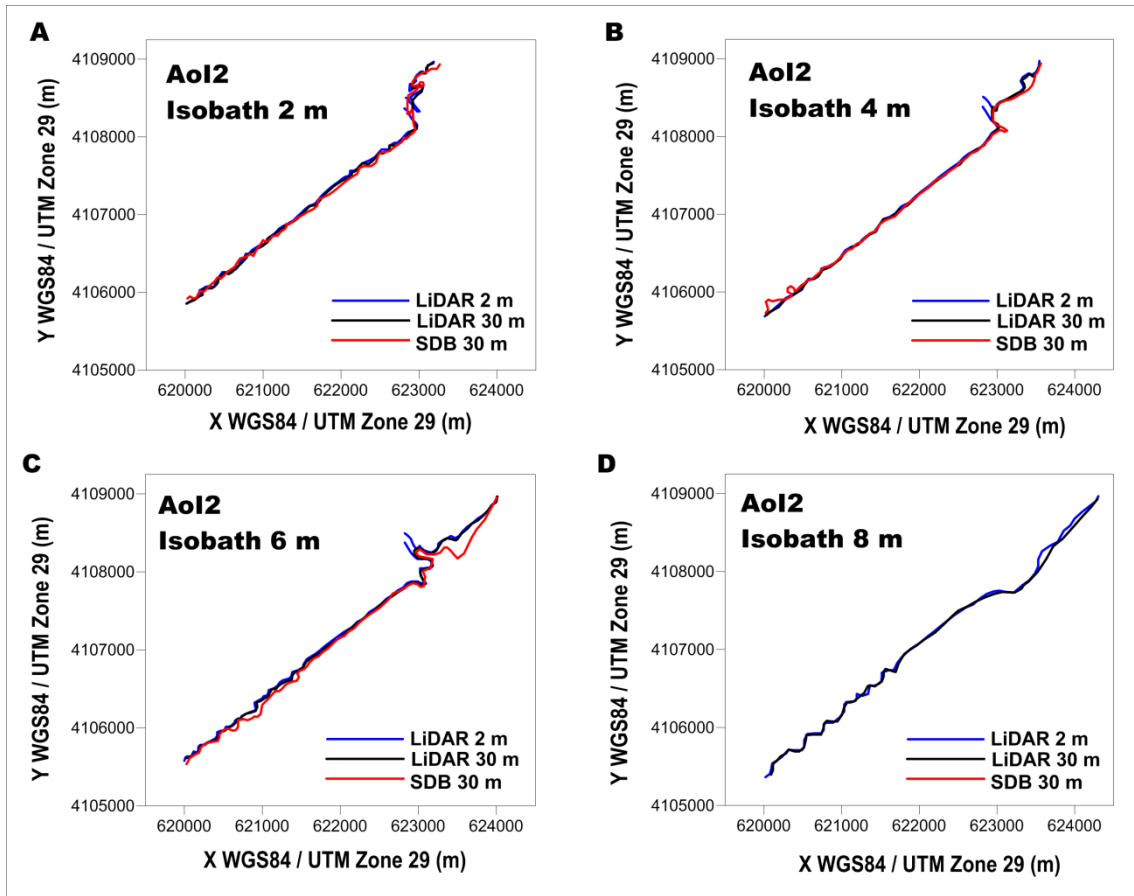
830

831

832

Figure 9. AoI2 nearshore cross-profiles spaced by 1000 m and extracted from bathymetric contour maps Bm1, Bm2, and Bm3.

833

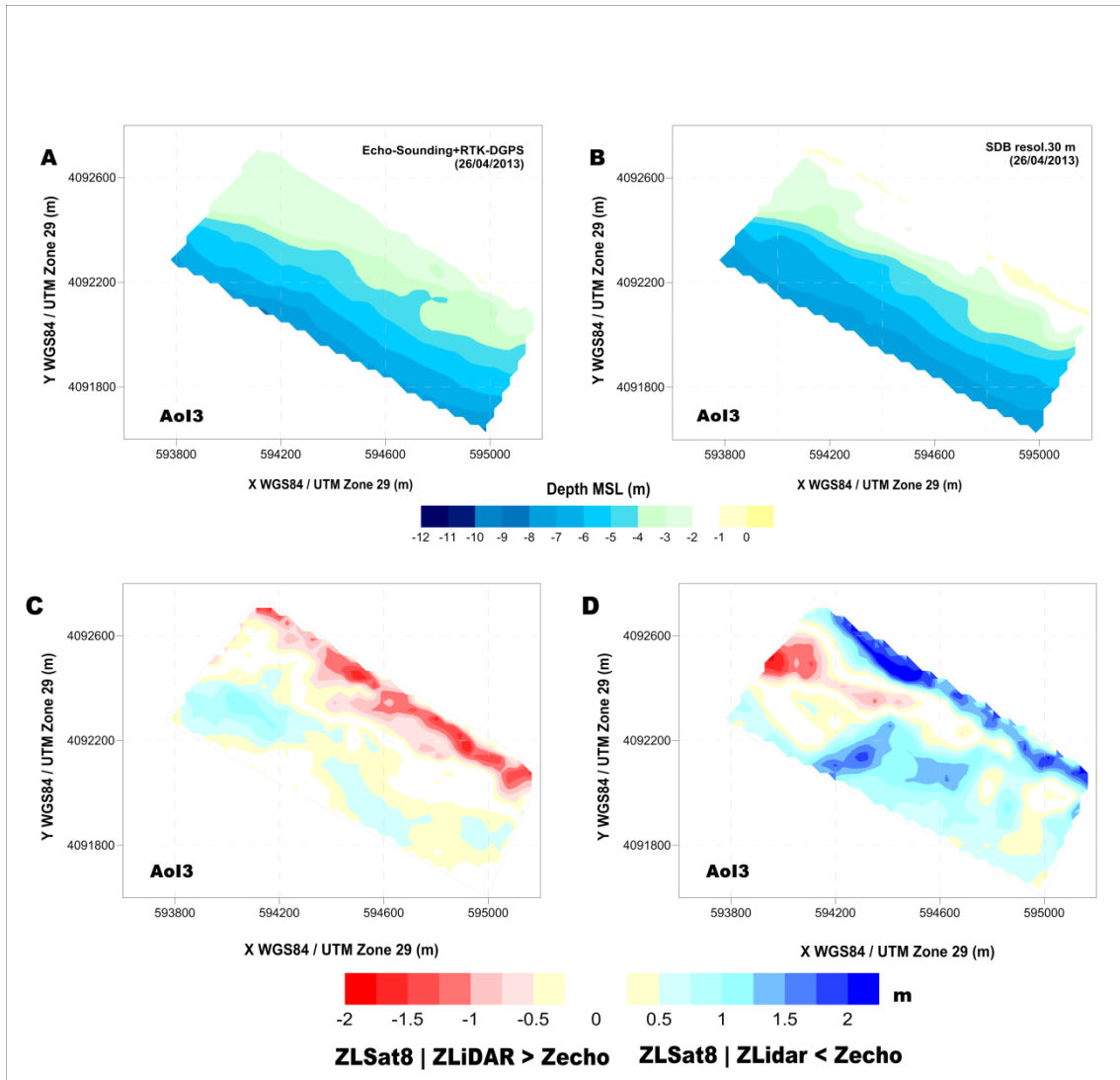


834

835 **Figure 10.** (A) 2-m, (B) 4-m, (C) 6-m, and (D) 8-m isobaths extracted from Bm1 (LiDAR 2m), Bm2
 836 (LiDAR 30 m), and Bm3 (SDB 30 m) for Aol2. XY coordinates are referred to WGS84 UTM29 and Z
 837 contour lines to MSL.

838

839

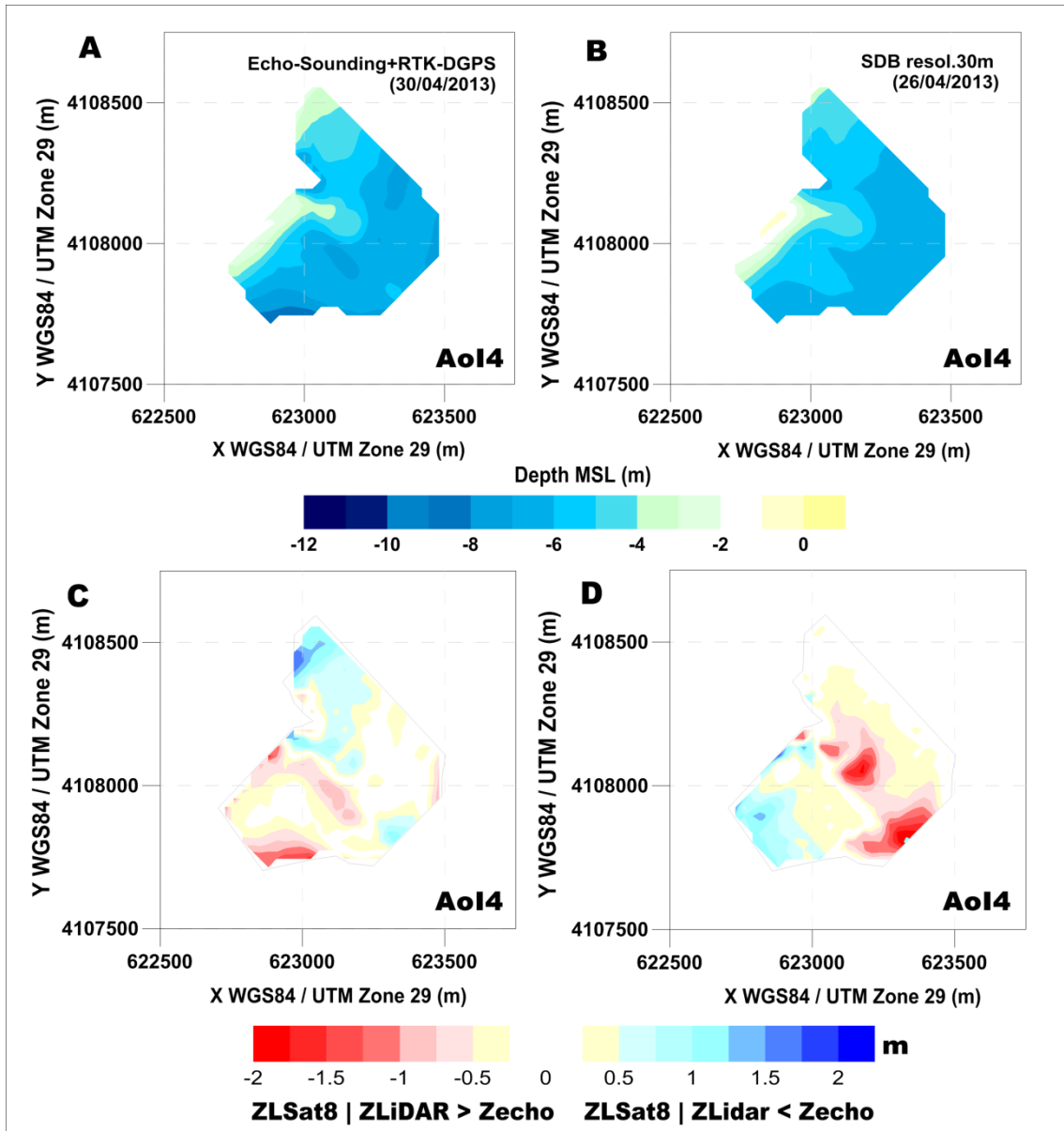


840

841 **Figure 11.** (A) AoI3 bathymetry contour map acquired using an echo-sounder synchronised with a RTK–
 842 DGPS in the area adjacent to Ancão Inlet on 26 April 2013. (B) Satellite-derived bathymetry (SDB)
 843 contour map (Bm3) with a 30-m resolution. (C) Difference map between A and B. (D) Difference map
 844 between LiDAR 05/2011 and SDB data derived from the Landsat 8 image of 26 April 2013; the red/blue
 845 values signify that accretion/erosion has occurred, respectively.

846

847



848

849 **Figure 12.** (A) AoI4 bathymetry contour map acquired using an echo-sounder synchronised with a RTK–
 850 DGPS in and around Tavira Inlet on 30 April 2013. (B) Satellite-derived bathymetry (SDB) contour map
 851 (Bm3) with a 30-m resolution. (C) Difference map between A and B. (D) Difference map between
 852 LiDAR 05/2011 and SDB data derived from the Landsat 8 image of 26 April 2013; the red/blue values
 853 signify that accretion/erosion has occurred, respectively.

854